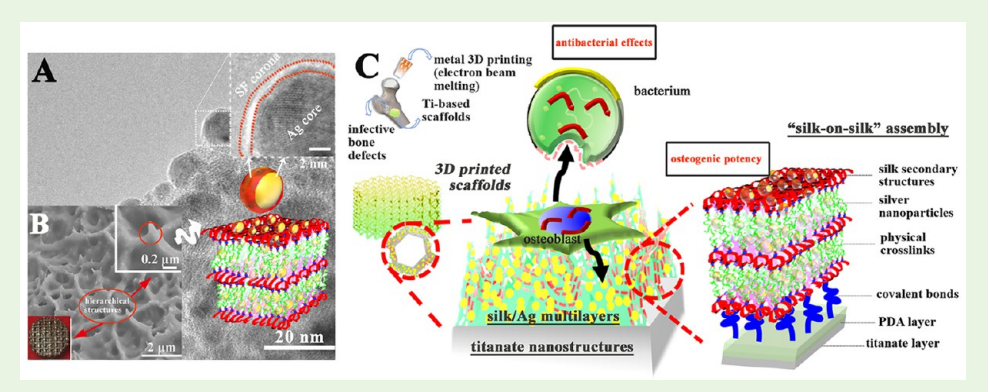


# Constructing Multilayer Silk Protein/Nanosilver Biofunctionalized Hierarchically Structured 3D Printed Ti6Al4 V Scaffold for Repair of Infective Bone Defects

Zhaojun Jia,<sup>†,‡,§</sup> Wenhao Zhou,<sup>‡</sup> Jianglong Yan,<sup>‡</sup> Pan Xiong,<sup>‡</sup> Hui Guo,<sup>†</sup> Yan Cheng,\*<sup>,‡</sup> and Yufeng Zheng\*,†,‡®

Supporting Information



ABSTRACT: Biomaterials-enabled regenerative medicine in orthopedics is challenged with infective bone defects that do not heal normally. Three-dimensional (3D) scaffold biomaterials simultaneously emulating skeletal hierarchy and eliciting sustainable osteogenetic and antibacterial functionalities represent a potent solution holding increasing fascination. Here we describe a simple combinatorial strategy for constructing such scaffolds. Fully porous titanium was first tailor-made by metallic powder 3D printing and subjected to in situ hydrothermal growth of a micro/nanostructured titanate layer, to which nanosilver encapsulated, physically cross-linked silk fibrin multilayer films were anchored through polydopamine-assisted, silk-on-silk selfassembly. The hydrophilicity, protein adsorption, and surface bioactivity of the scaffolds were investigated. Employing clinically relevant pathogenic Staphylococcus aureus bacteria, we tested that the silver immobilized scaffolds not only reduced adherence of bacteria on the surface, they also actively killed those planktonic, and these performances were largely maintained over an extended period of 6 weeks. Additionally, our engineered scaffolds were amenable to 14 days' continuous, intense bacterial attacks showing little sign of biofilm colonization, and they were interestingly capable of eradicating bacteria in already formed biofilms. High cargo loading, durable topical Ag+ release, and overwhelming oxidative stress were shown to contribute to this sustainable antibacterial system. Irrespective of certain degree of cellular stress at early stages, our scaffolds elicited generally enhanced cell proliferation, alkaline phosphatase enzyme production, and matrix calcification of osteoblastic MC3T3-E1. These multifunctionalities, coupled with the design freedom, shape flexibility, and cost-effectiveness offered by 3D printing, make our scaffold biomaterials a promising option for customized restoration of complicated infective bone defects.

KEYWORDS: additive manufacturing, porous titanium, silk fibrin, silver nanoparticles (AgNPs), biomimetic, antibacterial, osteogenic

# 1. INTRODUCTION

In the past few decades, regenerative orthopedic medical devices, a kind of synthetic bone substitutes, have been extensively investigated as an accessible, affordable, and safe alternative to natural grafts for the correction, repair, and replacement of large unhealable bone defects in occasions such as trauma, abnormalities, nonunion fractures, infections, and tumor resection. 1-3 Nevertheless, there are unmet or unattended clinical needs such as mismatched mechanical

properties between devices and surrounding bones,4 lack of tissue regeneration and implant fixation,<sup>3</sup> and complex reconstructive surgeries.<sup>5</sup> On the other hand, the almost inevitable biomedical device-associated infections (BAIs) have posed critical challenges in the reconstruction of infective large

Received: July 26, 2018 Accepted: September 17, 2018 Published: September 17, 2018



<sup>&</sup>lt;sup>†</sup>Department of Materials Science and Engineering, College of Engineering, Peking University, Beijing 100871, China

<sup>&</sup>lt;sup>‡</sup>Center for Biomedical Materials and Tissue Engineering, Academy for Advanced Interdisciplinary Studies, Peking University, Beijing 100871, China

<sup>&</sup>lt;sup>§</sup>Department of Orthopaedic and Traumatology, The University of Hong Kong, 21 Sassoon Road, Pokfulam, Hong Kong, China

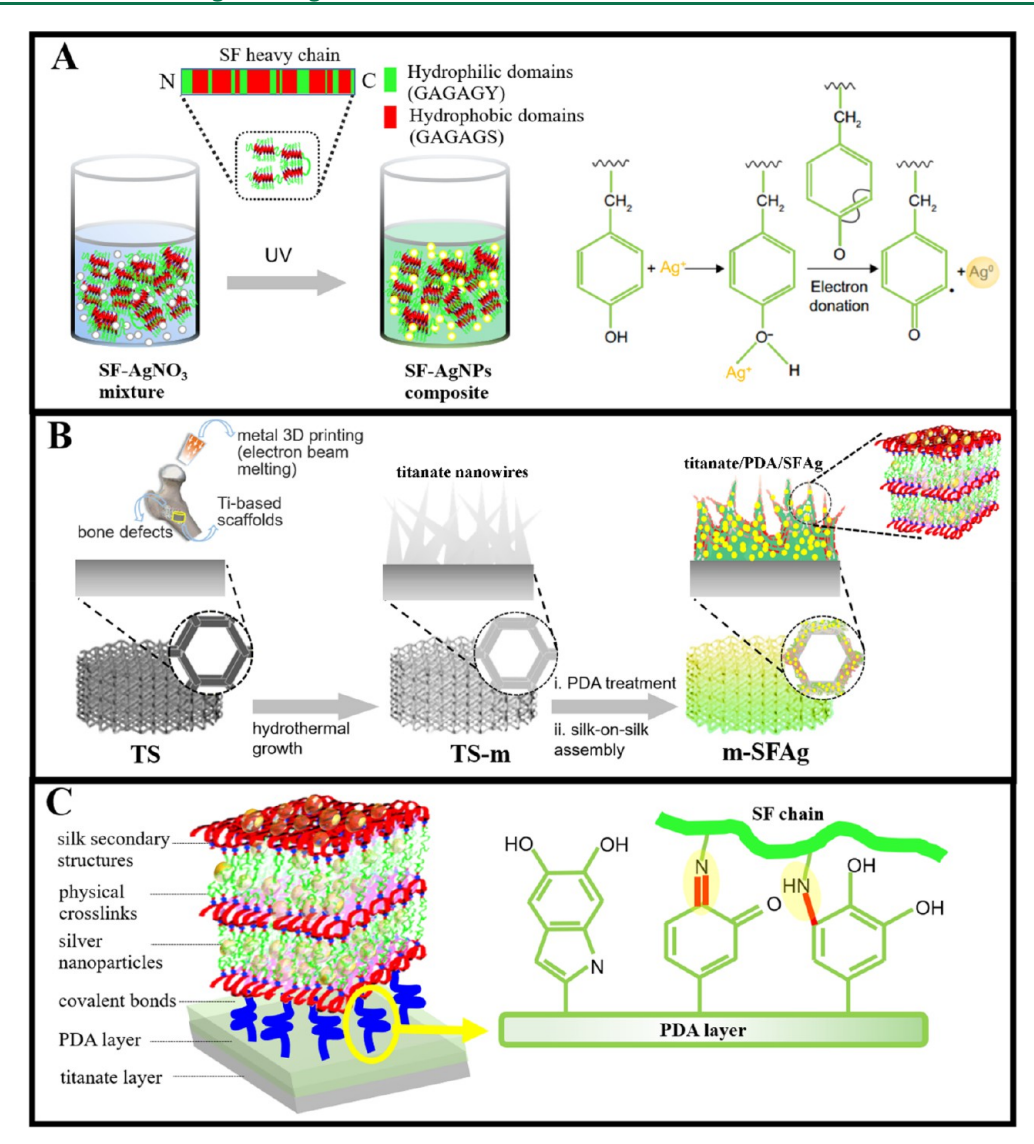


Figure 1. (A) Synthesis route of SFAg composite (left) and proposed mechanism of the reduction of Ag<sup>+</sup> ion by Tyr residues in silk chain<sup>20</sup> (right). (B) Schematic of the combinatorial strategy for constructing the hierarchically biomimetic and biofunctionalized scaffolds. (C) Schematic of the envisioned m-SFAg architecture and possible interactions among different coating components. Here, a titanate layer is hydrothemally grown in situ from porous TS, upon which a self-polymerized PDA layer is tightly adhered. The PDA reacts with silk precusor layer via Michael addition or Schiff base kinetics, <sup>24,26</sup> thus covalently grafting the latter. Multiple SFAg layers are constructed through silk-on-silk assembly and held together by physical cross-links of silk secondary structures such as β-sheets. <sup>22,32</sup> Simutaneously, nanosilver is encapsulated with SF chains and fully embedded within the multilayed matrix.

bony defects.<sup>6,7</sup> These motivate the development of more rationally designed multifunctional biomaterials with adaptive mechanical properties and geometry, enhanced osteointegration performances, and exceptional infection-resistant/-combating functionalities.

Nowadays, powder-based 3D printing techniques such as electron beam melting (EBM) and selective laser melting (SLM), are gaining increasing attention for customized design and rapid and precise fabrication of metallic scaffolds (e.g., porous titanium) with geometrical and mechanical suitability for bone tissue adherence and ingrowth. In contrast to their solid counterparts, such implants hold an inviting prospect touching their adjustable size, shape and porosity, tailored elastic modulus and strength, sufficient space allowing bone and blood vessel to grow into, and open channels facilitating mass transport and nutrient supply. 1,5 Nevertheless, the asmanufactured parts are still far from satisfactory pertaining to

their insufficient bioactivity and biointegration ability and deficiency in anti-infection capacities, all of which are central to the ultimate success of an orthopedic implant.<sup>6</sup> Fortunately, a new paradigm has emerged for introducing such functionalities additionally post fabrication through facile surface treatment (e.g., acidic/alkaline etching and oxidization) or chemical functionalization at micro/nanoscale utilizing the vast macrospace and surface area of the porous architectures.<sup>8,9</sup> Particularly, many studies have disclosed that, besides the roles of macroporous structures, micro/nano dimensional and biochemical cues on the surface emulating the exact contexts of bone extracellular matrix (ECM) also contribute to osteogenesis/osteointegration.<sup>3,10</sup> In return, the forgoing hierarchical constructs behave as a potent vehicle of functionalized antimicrobials to impart localized, strong yet sustainable antibacterial effects. With respect to antimicrobials, inorganic particulate antimicrobials such as nanosilver (i.e., AgNPs) are much preferable because of their intriguing characteristics such as slowly oxidizing nature, broad bactericidal spectrum, strong oligodynamic effect, and low incidence of drug resistance. <sup>9,11</sup>

Driven by the above paradigm, in this study, highly porous Ti6Al4 V scaffolds shall be first printed via EBM demonstrating designer macroscopic hexagonal unit cells of alloy struts interconnected with each other. Second, on the strut walls of the metal template, microscaled, nanowire-shaped titanate bioscaffolds shall be hydrothermally grown from substrate titanium in situ. Furthermore, assisted by the versatile musselinspired polydopamine (PDA) chemistry, nanosilver encapsulated silk fibrin (SFAg) will be robustly anchored over onto the titanate scaffold backbone through aqueous self-assembly to form multilayers while generally retaining the underneath nanowire morphology, eventually yielding a fully integrated titanate/SFAg hybrid architecture (Figure 1).

In this design, the 3D printed mesh titanium and nanowire shaped titanate recreate the dimensional and topographical contexts of native bone tissue, while silk fibrin (SF), a natural fibrous protein extracted from Bombyx mori (B. mori) silkworms, is expected to afford chemical similarity to the bony ECM components. SF in its essence is a hierarchical nanofibril self-assembled from native silk proteins, 12 which depicts resemblance of fibrillar ECM collagen at nanoscale, thus adding osteogenetic cues. There are more reasons backing SF up: (1) SF is born a biomaterial for bone regeneration with fascinating features such as good biocompatibility, outstanding mechanical properties, adjustable biodegradability, and ease of processability; 13,14 (2) SF is capable to regulate the crystallization of hydroxyapatite (HA) in (simulated) biological milieus; 15,16 (3) The peptidic nature of SF represents biorecognition cues for instructing cellular proliferation and differentiation; 16,17 (4) SF harbors diverse side chain chemistries as cargos for localized delivery of macromolecules and drugs with tunable liberation characteristics, 18,19 and as biotemplates for synthesis of inorganic nanomaterials with controllable morphology and polymorphs.<sup>20</sup> Especially, the electron donating tyrosine (Tyr) residues in SF are believed to account for the in situ chelating and reduction of Ag+ into nanosilver, 11,20,21 a process that can be further accelerated by light exposure, yielding relatively stable SFAg aqueous dispersions (Figure 1A).

Pleasingly, the as-generated SFAg dispersions are readily applicable for sequence-specific silk-on-silk construction of multilayer structures on substrate, wherein physical crosslinking (majorly via  $\beta$ -sheets) and hydrophobic—hydrophobic interactions occur between one layer and another. 22 Moreover, these SFAg multilayers are anchored tightly onto the titanate undercoating via a bridge molecule PDA that is formed at first on titanate through pH triggered self-polymerization of monomer dopamine (DA).<sup>23</sup> The catechol-bearing PDA possesses substrate independent adhesivity and is known as a multifunctional secondary reaction platform toward various functional groups such as quinone, thiol, amine, etc. 23,24 In particular, PDA can react with SF biomaterials through Michael addition or Schiff base between amine groups of PDA and amide groups of silk.<sup>25,26</sup> Note also that the titanate nanowire as grown serves as both a natural framework to which SFAg multilayers cohere (mediated by PDA) and a conceptual mimic of host bony microstructures such as lamellae and osteons eliciting tissue microenvironmental cues.<sup>27</sup> Meanwhile, the multilayer SFAg is a localized depot and delivery platform of Ag+ ions whose sustained active release can impart

exceptional durable antibacterial and antibiofilm activities to the constructs. Thereby, in this way, a designer silk protein/nanosilver multilayer biofunctionalized, hierarchically structured 3D printed scaffold system is established (Figure 1B, C). Expectedly, such a system can render the restoration of bone defects even with contaminations by first scavenging potential pathogens and then orchestrating the tissue healing process.

The present study set out to produce the said scaffolds and investigate their potential as a personized therapeutic tool for infective bone defects. The resultant scaffolds were characterized or tested with regard to macro/microstructures, chemical composition, hydrophilicity, and protein affinity. Besides, the bone bioactivity of the scaffolds was evaluated using an in vitro biomineralization test. Multiple antibacterial/ anti-infective behaviors of the scaffolds against a clinically relevant Staphylococcus aureus (S. aureus) bacteria strain were investigated systematically, with emphasis on the antibacterial efficacy and its longevity and impacts on biofilm formation and established biofilms. Preliminary insights into the antibacterial mechanisms were provided in terms of Ag+ ion release and generation of reactive oxygen species (ROS) and surface nanostructures' effects. Furthermore, the capacity of the engineered scaffolds to behave as a 3D framework for supporting osteoblast growth and inducing osteogenic signals was examined by cultivation of osteoblastic MC3T3-E1.

#### 2. EXPERIMENTAL SECTION

**2.1. Scaffold Preparation.** 2.1.1. 3D Printing of Scaffolds. Ultrafine alloy powders (45–100  $\mu$ m; 4.3 g cm<sup>-3</sup> in density) of Ti6Al4 V were used to fabricate hexagonally periodic porous scaffolds via EBM,<sup>2</sup> as schematically illustrated in Figure S2. In brief, a 3D model of the scaffolds was generated through computer aided design (CAD) (Step 1), and it was then converted into STL data that controlled the EBM machine (Arcam AB, Sweden) (Step 2). In a third step (i.e., 3D printing), computer-manipulated high-energy electron beams (maximum power 6 kW) scanned over the alloy powders and selectively melted them (which occurred in a built platform (bed) in a vacuum chamber ( $<5 \times 10^{-4}$  mBar)), forming interconnected mesh networks in a layer-upon-layer fashion. Afterward, the as-manufactured scaffolds underwent intensive powder blowing and sonication to detach loose particles and remove pollutants and were denoted as TS. The resultant cylindrical scaffolds ( $\Phi$ 10 mm × H5 mm) had an open porous structure and diamond-like lattice, as interconnected by 400- $\mu$ m-thick alloy struts; the pore size was 682  $\mu$ m and the porosity was about 73%.

2.1.2. Surface Treatment and Functionalization. To produce the micro/nanostructured scaffolds (m-TS), we subjected the TS samples to alkali-heat-treatment in a NaOH solution (1.25 M) at 120  $^{\circ}\text{C}$  for different time, followed by thorough rinse in deionized water (DI) at 60  $^{\circ}\text{C}$  to reach neutral conditions. Subsequently, these samples received a prelayer of PDA through a facile spontaneous polymerization of monomer DA.  $^{23}$  Typically, the intermediate scaffolds were immersed into a Tris–HCl buffer (10 mM, pH 8.5) of dopamine hydrochloride (Sigma) at 2 mg mL $^{-1}$  for 4 h to endow their surfaces with a significant number of catechol/amino groups to facilitate silk molecule anchorage.

To fabricate multilayer silk biofunctionalized scaffolds, the PDA-modified scaffolds (m-PDA) were dipped into freshly prepared SF or SFAg solutions for 10 min, secondary to thrice DI rinse (to get off redundant SF<sup>26</sup>) and to hot-air drying for 5 min (to induce  $\beta$ -sheet intersecting and interlayer cohesion<sup>22</sup>). By this way, one layer of silk-based thin film was formed. Analogously, a next silk layer was further deposited, based on the "silk-on-silk" self-assembly principle.<sup>22</sup> The entire procedure was repeated. The SF and SFAg functionalized scaffolds were denoted as m-SF and m-SFAg, respectively. Hereby, aqueous SF solution was extracted from *B. mori* cocoons following a previous protocol.<sup>13</sup> Briefly, the ends of the cocoon were snipped and

the silkworm chrysalises were removed. The resultant cocoons were degummed in boiling solution of 0.02 M Na<sub>2</sub>CO<sub>3</sub> for 30 min. The remaining fibroin fibers were rinsed, dried, and dissolved in 9.3 M LiBr solution and subsequently the salts were removed by dialysis (MEMBRA-CEL, 12000–14000 MWCO) against DI for 3 days. The purified SF was centrifuged and the supernatant was collected. The final SF solution (7–8 wt %) was stored at 4 °C and diluted to 0.5 wt % for use. To prepare SFAg solution, the diluted SF solution was added with AgNO<sub>3</sub> (0–25 mM) to result transparent mixtures that were thereafter exposed to UV light ( $\lambda$  = 254 nm, 40 W) for further reduction.

- **2.2. Surface Characterization.** The microstructure and surface morphology of samples were characterized by field-emission scanning electron microscopy (FE-SEM, S-4800, Hitachi) and transmission electron microscopy (TEM, H-9000NAR, Hitachi). For determining chemical composition and structure, energy-dispersive X-ray spectrometry (EDS), X-ray diffraction (XRD, D8 Focus, Bruker), X-ray photoelectron spectroscopy (XPS, Kratos), and microscopic Fourier transform infrared spectroscopy (Micro-FTIR, Thermo Fisher) were employed. UV—vis spectra of the SF and SFAg were collected by a Hitachi U-2910 spectrophotometer.
- **2.3.** Ag<sup>+</sup> Ion Release. Specimens were immersed in triplicate in phosphate buffer solution (PBS, pH 7.4) at 37 °C under dark and static conditions. At selected time points, the entire volume was collected and refilled with fresh PBS accordingly. The release profiles were determined through analysis of Ag<sup>+</sup> concentrations using inductively coupled plasma-atomic emission spectrometry (ICP-AES, Leeman, USA). Additionally, the total Ag content was obtained by sampling in 4% dilute nitric acid.
- **2.4. Contact Angle (CA) Measurement.** Static CAs were obtained on a SL200B contact angle system (Kino, USA) at ambient conditions using the sessile drop method. Given the macroporous geometry of the scaffolds, relative measurements were done using asprinted and -treated TS solid plates ( $\Phi$ 10 mm  $\times$  H2 mm) instead. Tests were performed in triplicate in 6 different positions of the same surface.
- **2.5. Protein Adsorption.** The protein adsorption efficiencies were assessed as previously described using bovine serum albumin (BSA) as model protein. Briefly, each scaffold type (n=3) was incubated with 1 mL of BSA/PBS solution  $(1~{\rm mg\cdot mL^{-1}})$  at 37 °C for 0.5, 1, and 2 h. The amounts of protein adsorbed were quantified spectrophotometrically through probing the concentration reduction of BSA within the original solutions using micro Bicinchoninic Acid (BCA, Thermo scientific) kits (wavelength: 570 nm). Alternatively, the scaffolds were subjected to an identical 2-h incubation in fluorescein isothiocyanate (FITC) labeled BSA (Sigma), followed by fixation with 4% paraformaldehyde (PFA) and visualization with a laser scanning confocal microscope (CLSM, Nikon ALR-SI).
- **2.6.** In Vitro Bone Bioactivity. The bioactivity of samples was evaluated by an in vitro apatite formation assay in simulated body fluids (SBF) at 37 °C, followed by SEM-EDS investigation. Each scaffold was soaked in 10 mL of SBF statically for 14 days, with solution refreshed every other day. The SBF was prepared according to the known procedure. <sup>28</sup>
- **2.7.** In Vitro Antibacterial Assessment. 2.7.1. Bacteria Culture. S. aureus (ATCC 25923) cells were chosen and cultured in Luria–Bertani (LB) broth under aerobic humid conditions. For subsequent assays, the overnight-grown and subcultured bacterial suspensions ( $2 \times 10^8 \text{ CFU mL}^{-1}$ ) were diluted to desirable concentrations.
- 2.7.2. Inhibition Zone Test. To perform the inhibition zone antimicrobial testing, we placed the sterilized scaffold samples (n=3) on LB agar plates which were covered with  $1\times 10^6$  to  $1\times 10^7$  CFU mL $^{-1}$  of S. aureus cells and incubated overnight at 37 °C. The biocidal activity of the scaffolds was identified and estimated as the diameter of an inhibition zone around. <sup>1</sup>
- 2.7.3. Determination of Bacterial Growth Curves. The growth curves of S. aureus bacterial cells exposed to different materials were examined in triplicate. The initial bacterial concentration was adjusted to approximately  $1 \times 10^5$  CFU mL $^{-1}$ . Bacteria/scaffold cultures were incubated in a shaking incubator at 37 °C for up to 24 h for the

bacteria to grow. Through repeated measuring the optical density (OD) at 600 nm as a function of time, growth curves of bacterial cells were thus obtained.

- 2.7.4. Antibacterial Efficiency with Sustainability. To evaluate the m-SFAg scaffolds' antibacterial efficiencies and their sustainability, bacterial suspensions ( $1 \times 10^5$  CFU mL<sup>-1</sup>) were introduced into 24-well polystyrene tissue culture plates (TCPS) containing sterilized scaffolds that had been prestored in PBS for scheduled time (0–6 weeks). After an incubated period of 12 h, the culture media was then sampled for counting of planktonic bacteria, while respective scaffolds were withdrawn, rinsed, and ultrasonically agitated to dislodge the adherent ones. The bacterial counts in both culture media and sonication suspensions were recorded by the spread plate method. The antibacterial rates ( $R_a$ ) with regard to planktonic bacteria in the culture media ( $R_{ap}$ ) and those for adhered bacteria on the specimens ( $R_{aa}$ ) were calculated per previous formula. Each test was repeated three times.
- 2.7.5. Anti-Biofilm Activity in Prolonged Culture. The scaffolds' abilities against biofilm colonization were assayed through a 14-d continuous exposure to harsh bacterial challenges ( $1 \times 10^8$  CFU mL $^{-1}$ ), with media changed twice a week. The biomass of adhered biofilms was quantified through staining them with 0.1% crystal violet, as detailed elsewhere. Meanwhile, SYTO 9/PI-based Live/Dead fluorescent staining of the bacteria within biofilms was implemented. For imaging, CLSM XYZ scan mode was utilized for acquisition of sliced images, which were later reconstructed into a 3D field of view. Results were confirmed by repeated imaging for at least 5 random positions.
- 2.7.6. Inactivation of Biofilm Bacteria. Model biofilms were established on commercially available pure titanium (cTi) foils. In brief, S. aureus cells  $(1\times10^8~{\rm CFU\cdot mL^{-1}})$  were inoculated uniformly onto substrates of cTi in 24-well TCPS and cultured at 37 °C for 48 h. The foils were transferred to new TCPS containing TS and m-SFAg. Prior to that, loosely adhered bacteria were removed with gentle PBS rinse. Fresh LB medium was filled and the constructs were allowed to incubate for another 24 h, followed by Live/Dead staining based CLSM study of the cTi specimens, as described above. The procedure was repeated three times.
- 2.7.7. Detection of ROS. The ROS generation during bacteria culture was evaluated through the degradation of 2',7'-dichlorofluorescein diacetate (DCFH-DA, (Jian-cheng Biotech, Nanjing, China). The nonfluorescent DCFH-DA compound reacts readily with ROS and produces strongly fluorescent dichlorofluorescein (DCF,  $E_x/E_m = 488/535$  nm). The DCF fluorescence intensity can be quantitatively correlated with the amount of ROS. In a typical test, dilute DCFH-DA was added to the scaffold-bacteria constructs and incubated at 37 °C for 30 min to yield ROS whose fluorescence intensities were quantified spectroscopically.
- **2.8. Cell Culture Studies.** 2.8.1. Cell Culture and Seeding. The preosteoblastic cell line MC3T3-E1 was cultured in  $\alpha$ -minimum essential medium ( $\alpha$ -MEM) supplemented with 10% fetal bovine serum (FBS) and 1% penicillin/streptomycin in a humidified incubator of 5% CO<sub>2</sub> at 37 °C. All sterilized scaffolds were placed in 24-well TCPS and preconditioned in medium for 30 min, and then 50  $\mu$ L of cell suspension (2 × 10 $^6$  cells mL $^{-1}$ ) was plated uniformly onto each of them. The culture complex was transferred latter to new TCPS and cultivated for up to 28 d. Medium change intervals were 2–3 d. All cell experiments were performed in triplicate (n = 3).
- 2.8.2. Cell Adhesion and Proliferation. For this part, a convenient CCK-8 Cell Count Kits (Dojindo, Japan) was used. <sup>10</sup> In an adhesion assay, cells were maintained in an incubator for 6 h to allow attachment, and the unattached ones were removed. The mitochondrial activities of adhered cells on scaffolds were determined and expressed as relative adhesion compared to those of the TS. Likewise, in proliferation assay, the seeded scaffolds were incubated routinely for 2 weeks, and the cell numbers were quantified at indicated time points.
- 2.8.3. Cytoskeleton and Spatial Growth. The MC3T3-E1 cytoskeleton on different scaffolds was visualized by CLSM. Briefly, samples were fixed by 4% PFA and then permeabilized with 0.1%

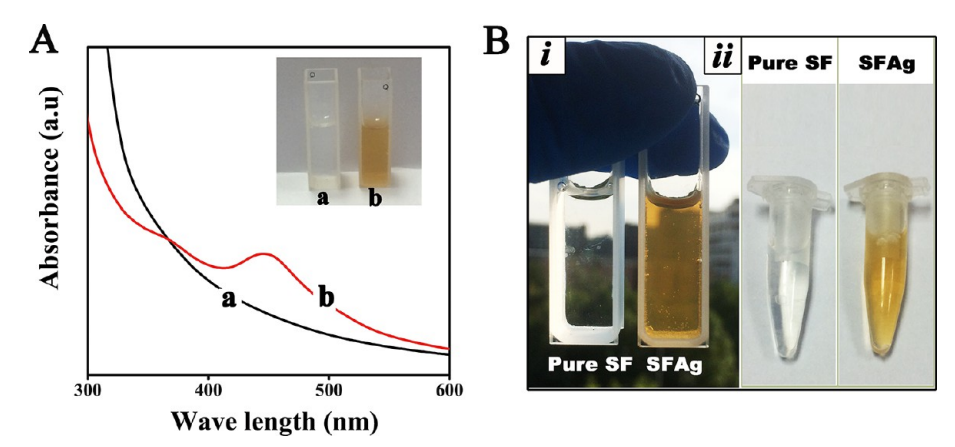


Figure 2. (A) UV—vis absorption spectra of (a) pure SF and (b) SFAg dispersion, inset with the digital photographs. (B) Transparency of the pure SF and SFAg against (i) an outdoor scene and (ii) the blank printer paper. Clearly, the pure SF is colorless and well transparent, whereas the SFAg displays a yellowish color and translucent nature.

Triton X-100 and double-stained with FITC-phalloidin (Invitrogen, 1:200) and DAPI (Sigma, 1:1000). The stained constructs were observed under CLSM in both XY and XYZ scanning modes to visualize the cytoskeleton development and spatial growth of cells.

2.8.4. Cytotoxicity and Cell Viability. For cytotoxicity evaluation, the degree of cell apoptosis was assessed through measuring the leakage of intracellular lactate dehydrogenase enzyme (LDH) by means of a LDH Kit (abcam, USA) in triplicate as per the manufactures' instructions (see details elsewhere  $^{10}$ ). Cells cultured on TCPS were set as negative control. For viability, cells were incubated with 2  $\mu$ M Calcein AM and 4  $\mu$ M PI (Dojindo, Japan) for 15 min and then subjected to CLSM imaging.

2.8.5. Osteodifferentiation Studies. The early osteodifferentiation potential of MC3T3-E1 on the scaffolds was evaluated in terms of alkaline phosphatase (ALP) activity at 7 and 14 d, based on the pnitrophenyl phosphate (p-NPP) method. 10 Briefly, aliquots of cell lysates were incubated with a buffered reaction solution comprising substrate p-NPP and then incubated at 37 °C to produce pnitrophenol (p-NP) whose concentrations were determined spectroscopically with reference to p-NP standards. The final ALP activity was standardized to the total intracellular protein content, as determined by the microBCA assay. To investigate the long-term osteogenic capacities, cells were cultivated on scaffolds for up to 28 d. The extracellularly deposited minerals were assayed using specific Alizarin Red S (ARS, Sigma) staining, as detailed elsewhere. In short, fixed cultures were stained with 2% ARS (pH 4.2) for 10 min and photographed after washing off unbound dyes. In addition, the dyes were eluted with 10% cetylpyridinium chloride for measurement of absorbance at 562 nm.

**2.9. Statistical Analysis.** All data were expressed as means  $\pm$  standard deviations (SD) and were analyzed using one-way variance analysis (ANOVA) or Student's t test, wherein p < 0.05 was considered statistically significant.

# 3. RESULTS AND DISCUSSION

**3.1. Preparation and Characterization of SFAg Composites.** In the study, silver releasing hierarchically biomimetic 3D bioscaffolds were easily fabricated through harnessing 3D printing, surface nanomodification and SFAg biofunctionalization. In other words, SFAg composite was synthesized in situ and applied through a facile self-assembly process initiated by the catechol chemistry of PDA onto the micronanostructured scaffold surfaces, thus yielding the hierarchically defined m-SFAg scaffolds. Here, the synthesis protocol of SFAg was adapted from prior studies. Tyr is among the 18 amino acid residues of *B. mori* SF, and it owns strong electron-donating property. Thanks to the electron-

donating characteristic of phenolic groups in Tyr (Figure 1A, right), either Tyr molecule itself or Try residue-containing polypeptides/proteins are able to immobilize and transform noble metal ions (e.g., Ag+ and Au+) into respective nanoparticles. Meanwhile, additional UV exposure was used to improve the reduction efficacy. Preliminarily, 0.5 wt % SF solutions were added with AgNO<sub>3</sub> powders at varying Ag concentrations (0, 0.5, 5, and 25 mM), and irradiated identically with UV light. A clear color change from colorless to yellow was witnessed, where the more the AgNO3 in solution, the darker the yellowish color was (Figure S1), implying an increasing amount of nanosilver yielded. Compared with transparent pure SF, the SFAg had a translucent nature (Figure 2B), likely due to the light absorption property of AgNPs. The UV-vis absorption spectra of pure SF and SFAg were shown in Figure 2A. Noticeably, unlike pure SF, a strong absorption band around 450 nm was seen for SFAg due to surface plasmon resonance (SPR) of AgNPs in the visible region,<sup>20</sup> validating silver reduction by UV light/SF side chains. Additionally, a small shoulder also emerged at 365 nm, which implicated coexistence of particulate silver of differing sizes or morphologies.<sup>20</sup> It should be pointed out that the yellowish colloidal solutions of SFAg were rather stable (with little sign of color change or aggregation) for weeks under storage at 4 °C. This suggests the additional roles of SF as dispersing and stabilizing agents and represents a key advantage in practical use versus conventionally synthesized AgNPs with high oxidizing and/ or aggregating tendency.<sup>20</sup>

**3.2.** Preparation and Characterization of the Hybrid Scaffolds. The thus-prepared SFAg aqueous solution was applied to the micro/nanostructured and PDA coated, 3D printed titanium scaffolds by means of stepwise self-assembly. Specifically, macroporous TS parts were first 3D printed layer upon layer via an EBM system (Figure S2). These parts ( $\Phi$  10 mm  $\times$  5 mm) demonstrated a highly porous structure with designer hexagonal unit cells (sized 682  $\mu$ m) (Figure S3). The unit cells were made up by interconnected 400- $\mu$ m-thick Ti6Al4 V alloy struts. The porosity was previously analyzed to be approximately 73%. These scaffolds subsequently received a simple hydrothermal reaction of alkali to grow in situ a macro/microporous nanowire bioscaffold, which is an alkali concentration dependent process involving novel solid-state chemistry and spontaneous nanotitanate growth and self-

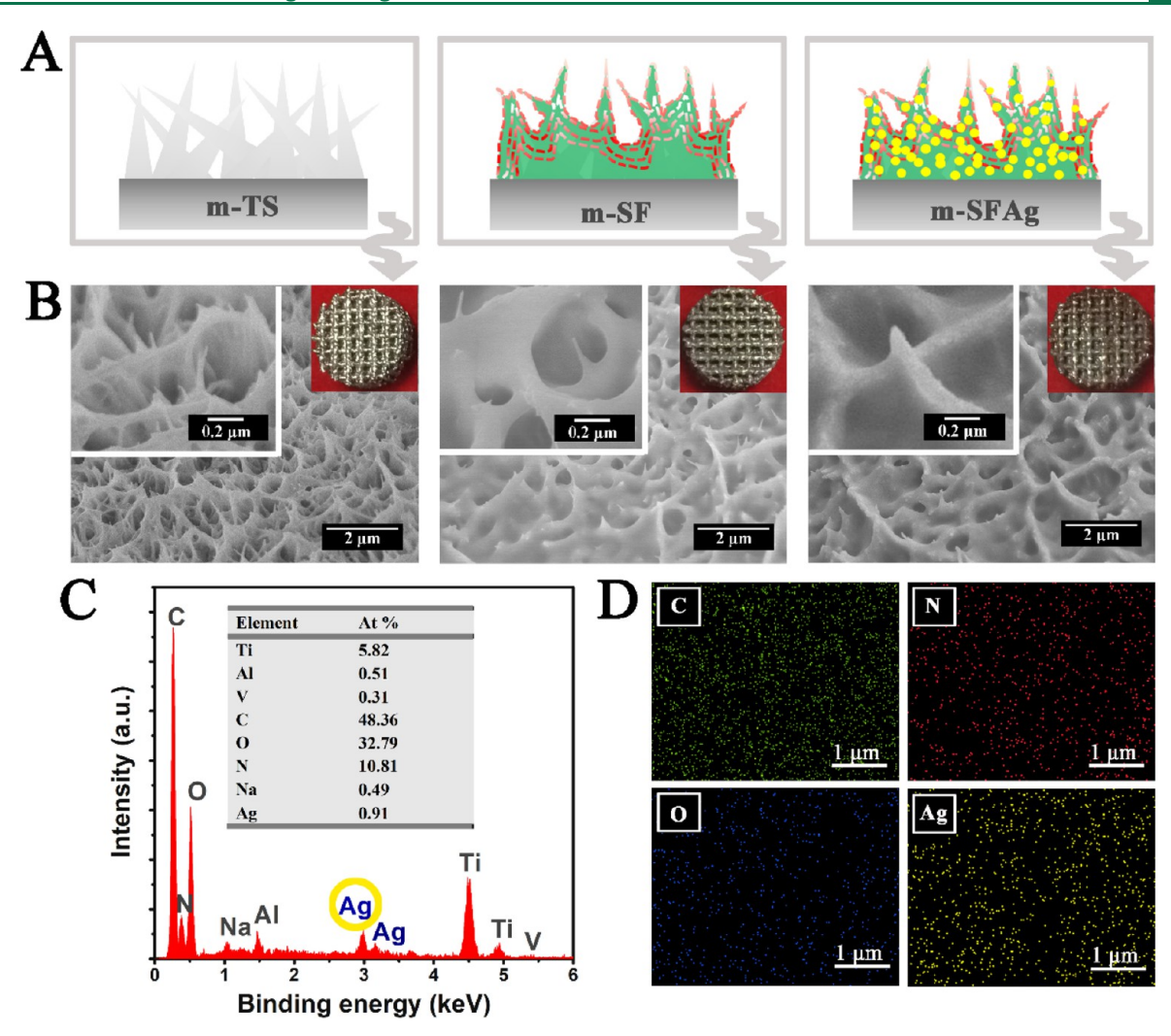


Figure 3. Scaffold surface characterization. (A, B) FE-SEM view (B) and relative schematic (A) of the m-TS, m-SF, and m-SFAg; left and right insets respectively show magnified images and macroscopic appearances of the scaffolds. (C, D) Selected area EDS (C) and elemental mapping (D) of the m-SFAg surface in B.

assembly (Figure S4).<sup>27</sup> Such bioscaffolds can act as an essential backbone or framework for subsequent assembling of silk multilayers, so as to create simultaneously the structural and chemical similarity to living bone tissues. Nevertheless, if polymeric SF is physically applied to a metallic or inorganic substrate, serious phase separation or delamination is likely to occur simply because of extremely bad interfacial compatibility in-between.<sup>26</sup> To circumvent this, we introduced an intermediary PDA nanolayer onto the porous m-TS surface via pH triggered self-polymerization of its monomer DA.<sup>23</sup> In fact, it has been shown that the mussel byssus derived PDA coheres preferably and stably onto Ti-based solid or porous substrata through strong bidentate coordination and that a PDA interlayer can serve as a versatile platform for further biofunctionalization of biomaterial surfaces. 2,10,30 Through a Schiff base or Michael-type addition pathway,<sup>24</sup> the oxidized phenolic hydroxyl(quinone) in PDA can react readily with the amines in SF, 26 as also illustrated in Figure 1C, thereby covalently immobilizing a precursor layer of SF or SFAg onto the hierarchical bioscaffolds. Following that, an extra thin layer of SF or SFAg was added right upon the silk precursor layer via dipping (into silk dispersions), drawing and rinsing, and then drying, during which silk proteins were absorbed and stabilized

by physical cross-links ( $\beta$ -sheets) and hydrophobic—hydrophobic interactions. <sup>22,32</sup> Of note, the rinsing and drying are essential steps because the former helped eliminate the loosely attached macromolecules, whereas the latter induced dehydration of hydrated hydrophobic domains and enhanced chain—chain contacts, culminating in stabilized secondary structures like  $\beta$ -sheets. <sup>33,34</sup> In addition, for the silver-impregnated SF matrix, the polymer—metal complexation might as well contribute to the multilayered coating structure. <sup>20,35</sup> One more silk layer was constructed likewise and robust multilayers of SFAg (or SF) were attained through simply repeating the procedures above.

Figure 3A, B illustrates and presents the microstructures and surface morphologies of the m-TS, m-SF, and m-SFAg. As we can see, the m-TS was a hierarchical bioscaffold featuring a microporous network configuration and nanowire topographical morphology (a mimic of bone hierarchy). Despite some degree of alteration to the nanowire topography, the PDA treatment and self-assembly of silk multilayers basically retained the hierarchical scaffold backbone, resulting in inorganic—organic hybrid bioscaffolds of m-SF or m-SFAg. Special note should be captured, however, that either too high SF concentrations or too many assembly cycles may otherwise

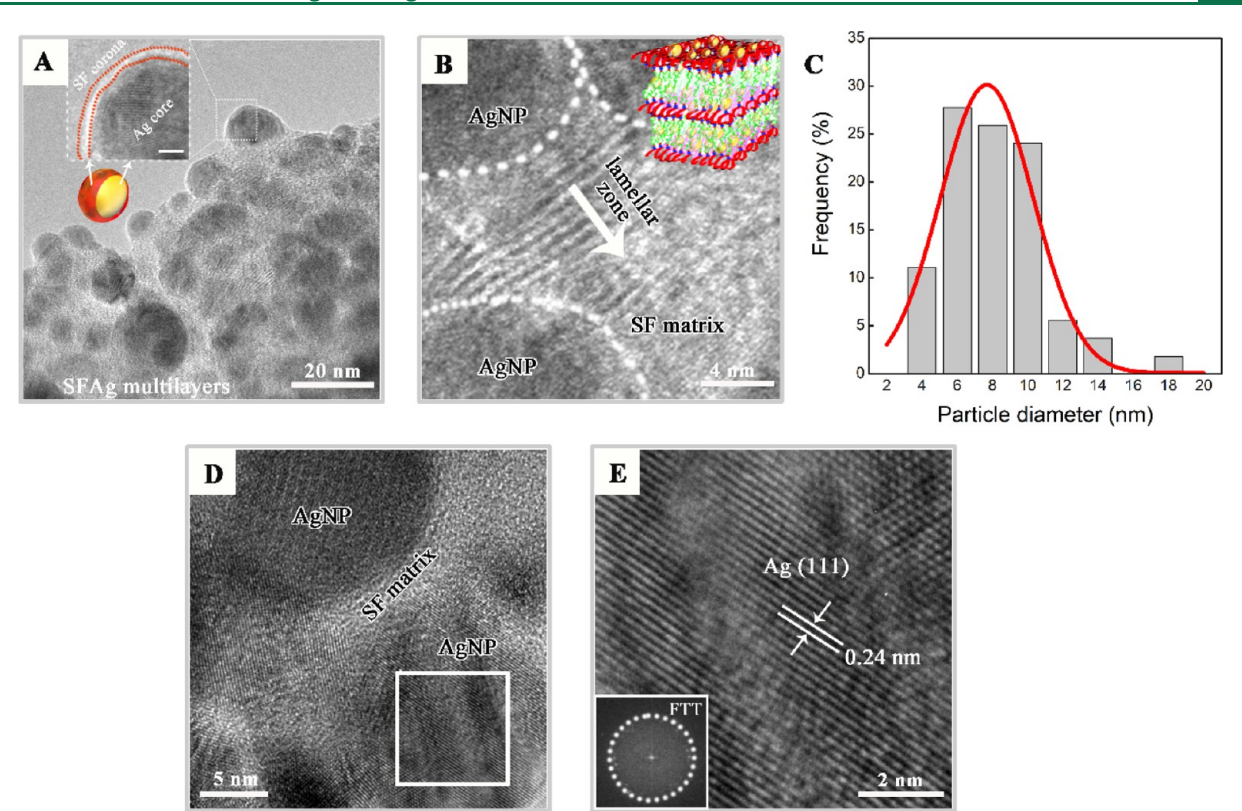


Figure 4. TEM microstructure of as-constructed SFAg multilayers. (A) Wide-area TEM image: relatively uniform AgNPs were closely packed within the SF matrix, and they were elaborately capped with SF nanolayers (inset image, edges outlined with red dashed lines; scale bar 2 nm) at closer examination, depicting a so-called "Ag core/SF corona" micellar structure (see also the inset 3D scheme). (B) High-magnification micrograph highlighting short-range ordered lamellar structures of SF multilayers, with white dashed lines outlining the nanosilver; (inset) a 3D scheme of the layered SFAg architecture. (C) Size distribution of AgNPs in A with a fitted curve. (D) HRTEM image of selected nanoparticles. (E) HRTEM image enlarged from the white rectangular region in D to manifest the lattice fringes of the crystal (inset, the FFT pattern), with the plane d-spacing measured to match the crystalline Ag structure.

deprive that biophysical cue, thereby destroying the intended hierarchy (Figure S5). A silk concentration of 0.5 wt % and assembly cycle of 5 was considered optimal and hence adopted throughout the context. For m-SFAg, nanosilver was not visible on surface according to direct SEM observation, probably due to the extreme particle sizes and poor conductivity of polymeric matrix. Nevertheless, EDS mapping in Figure 3D undoubtedly revealed the uniform distribution of elemental silver within the entire multilayer section. Moreover, surface presence of 0.91 at. % Ag was semiquantitatively determined (Figure 3C).

In addition, TEM images in Figure 4 disclose the microstructure and particle distribution of AgNPs within the silk multilayers. The dark particles with high electron cloudy density and surrounding dim substance were ascribed to AgNPs and SF films, respectively. Particulate Ag was relatively homogeneously distributed and exhibited typical sphere shapes and was capped with SF outer layers in nanometer thickness, resulting in a so-called "Ag core/SF corona" micellar structure (Figure 4A). Interestingly, special lamellar structures with short-range order were identified for the multilayers by increasing the magnification (Figure 4B), which was ascribed to the aligned secondary configurations of  $\beta$ -sheets of self-assembled silk backbone. This serves as valid evidence that physical cross-links by  $\beta$ -sheets, as illustrated in Figure 1C, should exist to integrate different multilayers of silk as a whole. The presence of  $\beta$ -sheets in silk is also suggested to facilitate Tyr ordering, thus resulting in well-dispersed, uniform AgNPs

with ultrasmall diameters.<sup>21</sup> The particle size distribution was statistically determined, ranging from 2 to 20 nm and averaged 7.1 nm (Figure 4C). According to the HRTEM images in Figure 4D, E, the lattice fringes were uniformly 0.243 nm (*d*-spacing of the crystallographic planes), which agreed well with the (111) plane of Ag (0) lattice parameters<sup>10</sup> and served as evidence to support that silver was presented in metallic form rather than as compounds. Taken all results together, hierarchically defined titanium scaffolds with well-integrated titanate/SFAg hybrid surface microstructure/chemistry were successfully fabricated.

XPS was employed to determine the chemical composition of TS, m-TS, m-SF, and m-SFAg (Figure 5A). The major surface elements of TS were Ti, O, and C, with the latter two arising from oxidization or contamination.<sup>2</sup> For m-TS, a specific Na KLL peak was observed corresponding to alkali treatment in NaOH solution. Pertaining to m-SF and m-SFAg, all substrate signals were shielded, whereas those for C 1s were apparently strengthened. In the meantime, a new strong band of N 1s emerged, ascribed primarily to silk protein and partly to PDA. Specifically, for m-SFAg, intensive sharp peaks of Ag were evident. Furthermore, the core-level XPS spectra of C 1s and Ag 3d for m-SFAg were fitted and given in Figure 5B, C. The C 1s band could be deconvoluted into three subcomponents: 284.8 eV (C-C/C-H), 286.1 eV (C-O), and 288.1 eV (C=O), correlating to different carbon contexts for SF. The Ag 3d showed the  $3d_{3/2}$  (368.4 eV) and  $3d_{1/2}$ 

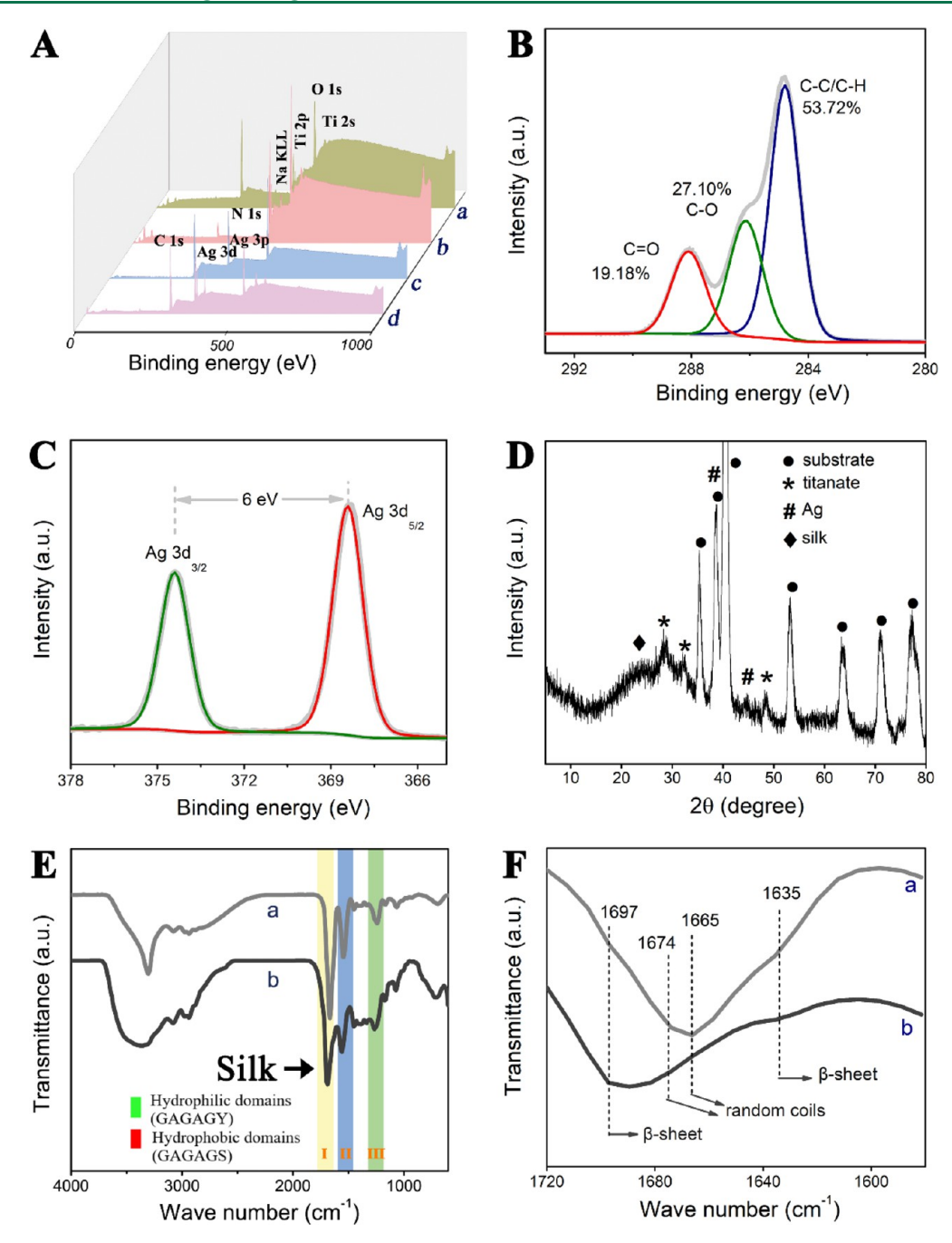


Figure 5. Chemical composition analysis. (A) XPS survey spectra of (a) TS, (b) m-TS, (c) m-SF, and (d) m-SFAg. (B, C) Core-level spectra of C 1s (B) and Ag 3d (C) for m-SFAg. (D) XRD pattern of m-SFAg. (E, F) FTIR spectra of m-SF (a) and m-SFAg (b).

doublet (374.4 eV) with a binding energy gap of 6 eV, which is characteristic of metallic silver (Ag (0)).

The phase structure of the m-SFAg was investigated by XRD, as presented in Figure 5D. The primary diffraction patterns arose from the metal substrate itself (titanium and titania). Besides that, the peak signals at  $2\theta$  of 28.5, 32.3, and 48.3° can be assigned to hydrated sodium titanate, correlating with the hydrothermal growth of nanowire structures. In addition, a defined broad halo diffraction peak belonging to the silk II form of SF, i.e.,  $\beta$ -sheet crystalline structure, was observed at  $2\theta$  of 23.7°, coinciding with the TEM results in Figure 4B and further validating the presence of physical cross-linking. Furthermore, small peaks located at 38.2 and 44.5°

were identified and assigned to the (111) and (200) planes of crystalline  $\mbox{Ag.}^{10}$ 

To clarify the existing chemical groups and secondary structures, and possible chemical interactions, micro-FTIR spectra were acquired for m-SF and m-SFAg (Figure 5E). The FTIR bands of SF are highly sensitive to the silk conformations and feature amide I, II and III bands of absorption. Both spectra demonstrated a distinct amide I band (1660–1700 cm<sup>-1</sup>), which belonged to the C=O bonds in the silk backbone coupled with the N-H bending and C=N stretching modes.<sup>22</sup> Additionally, characteristic bands of SF at 1543 cm<sup>-1</sup> (amide II) and 1250 cm<sup>-1</sup> (amide III) were assigned to C-N stretching coupled with N-H deformation and C-N stretching, respectively.<sup>15,31</sup> A close-up of the 1600–

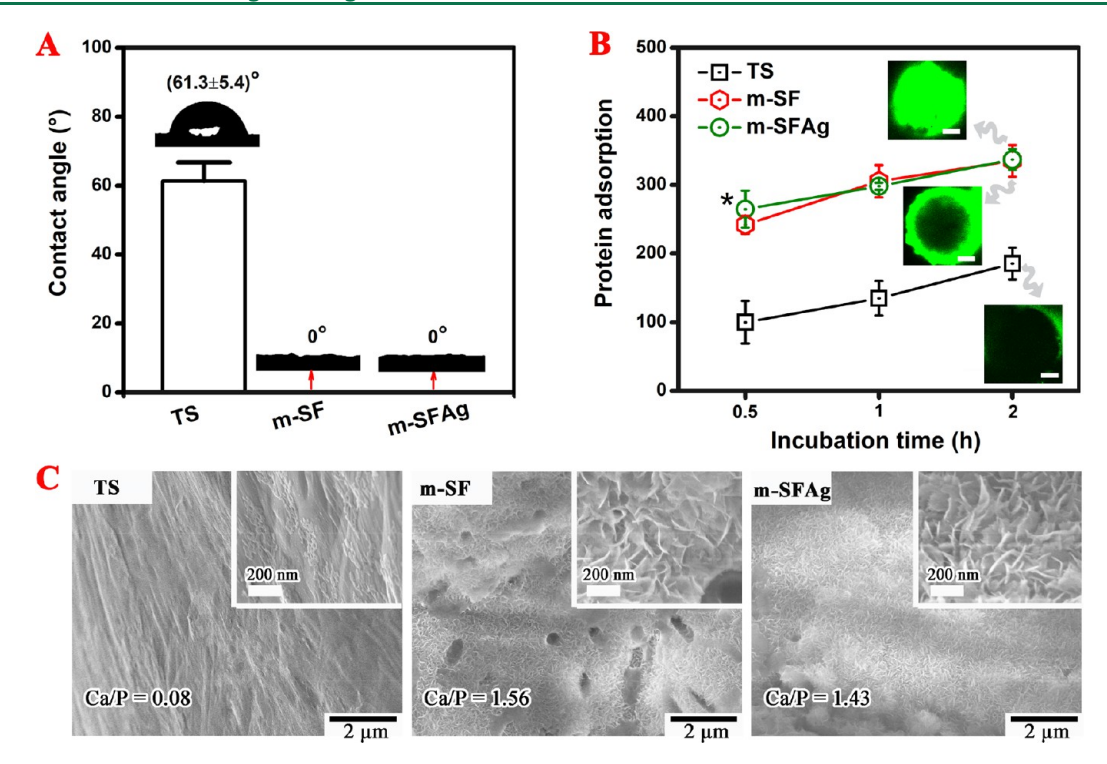


**Figure 6.** Surface properties of different scaffolds. (A) Hydrophilicity by CAs. (B) Protein adsorption curves as a function of time; (inset) typical fluorescence images of FITC-BSA (scale bare 20  $\mu$ m). (C) FE-SEM images showing apatite formation in SBF.

1720 cm<sup>-1</sup> infrared region was given in Figure 5F, wherein four sub-bands associated with the secondary conformations of silk were further distinguished: the two centered at 1635 and 1697 cm<sup>-1</sup> corresponded to crystalline  $\beta$ -sheets, whereas the other two at 1674 and 1665 cm<sup>-1</sup> were attributed to random coils. Notably, as compared to the m-SF, the m-SFAg had more  $\beta$ -sheets and fewer random coils, suggesting the potential impacts of silver on the conformational transformation of silk and possible interplays between SF chains and silver. It should be mentioned also that the  $\beta$ -sheets are essential for SF to maintain its fibrous structure (i.e., silk fibers) and exceptional mechanical properties, and to trigger physical cross-linking that integrates all SF components as a monolithic system.  $^{15,22,32}$ 

**3.3. Surface Wettability.** Implant biomaterials interplay with biological systems primarily via their surfaces. Biomaterial surface characteristics such as wettability are known to affect serum protein adsorption and substrate adhesion behaviors of osteoblastic cells and bacteria. The degree of surface wettability of an investigated material is often indicated by sensitive water CA analysis. The CA measurements for the TS, m-SF, and m-SFAg specimens were given in Figure 6A. In line with other titanium substrates,  $^{30,39}$  the as-printed TS showed a relatively hydrophobic surface character (CAs:  $61.3 \pm 5.4^{\circ}$ ). In stark contrast to that, water droplets spread out rapidly on the modified surfaces and fully covered them, giving CAs close to  $0^{\circ}$ , i.e., superhydrophilicity. This was majorly attributed to the super wetting effect of the microporous nanowire structures and seemed independent of silk modification.

**3.4. Protein Absorption Capacity.** Serum protein adsorption plays a central role in regulating the scaffolds' biological properties through mediating efficient membrane integrin recognition, thus influencing initial cell attachment after in vivo implantation. Employing BSA as model serum protein, we intended to distinguish the protein affinities of different scaffolds. First, micro-BCA measurement of protein

contents was done and the result is disclosed in Figure 6B. The adsorbed protein amounts increased with time for all groups. Delightedly, proteins adsorption on both m-SF and m-SFAg was favorably high when confronted to TS. This tendency was also ascertained by fluorescent BSA adsorption and CLSM visualization (Figure 6B, insets).

It is well-demonstrated that a biomaterial's capability of retaining protein is dependent on its surface wettability, composition, and topography (roughness). As given in Figure 6A, the hydrothermally treated and PDA/silk functionalized constructs were super more hydrophilic than TS, and this property may have assisted in elevating the amount of adhered proteins. Besides, we should not underrate the effects from the as-mentioned exceptional surface area and gorgeous hieratical architecture, along with the side chain chemistry of silk protein, when interpreting the augmented protein retaining capacity.

**3.5.** In Vitro Bioactivity. Bioactivity dictates a biomaterial's ability to bond with bone tissue. It is recommended that this ability be well=correlated to the apatite formation on the material's surface in vitro employing an acellular solution called SBF whose ion concentrations are akin to those of human blood plasma. The bioactivity of the scaffolds after immersion in SBF at 37 °C was thus examined.

Figure 6C reveals the apatite deposition on TS, m-SF, and m-SFAg surfaces. After 14 days of incubation, the TS surfaces remained almost intact laying only a few amorphous compounds, with a Ca/P ratio of 0.08. By sharp contrast, the surfaces of m-SF and m-SFAg were entirely covered with dense coatings of mineralized apatite crystals, which at high magnification featured representative "petal shaped" morphologies of bone-like apatite. Notably, the Ca/P ratio was determined as 1.56 and 1.43, respectively, for m-SF and m-SFAg, approaching that of hydroxyapatite in natural bone (1.67). Putatively, such impressive bioactive response was derived from the unique structural of *B. mori* silk. There are

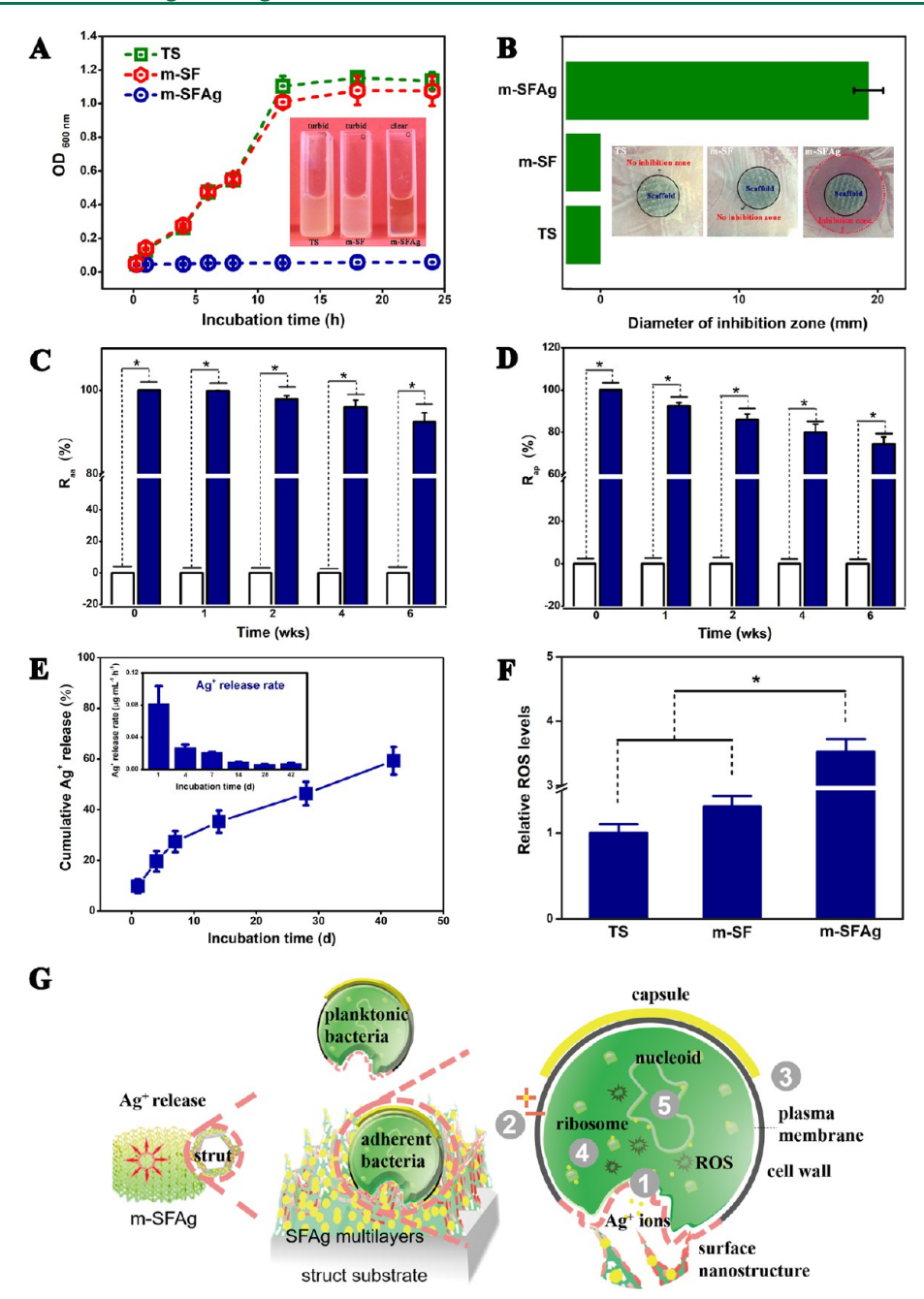
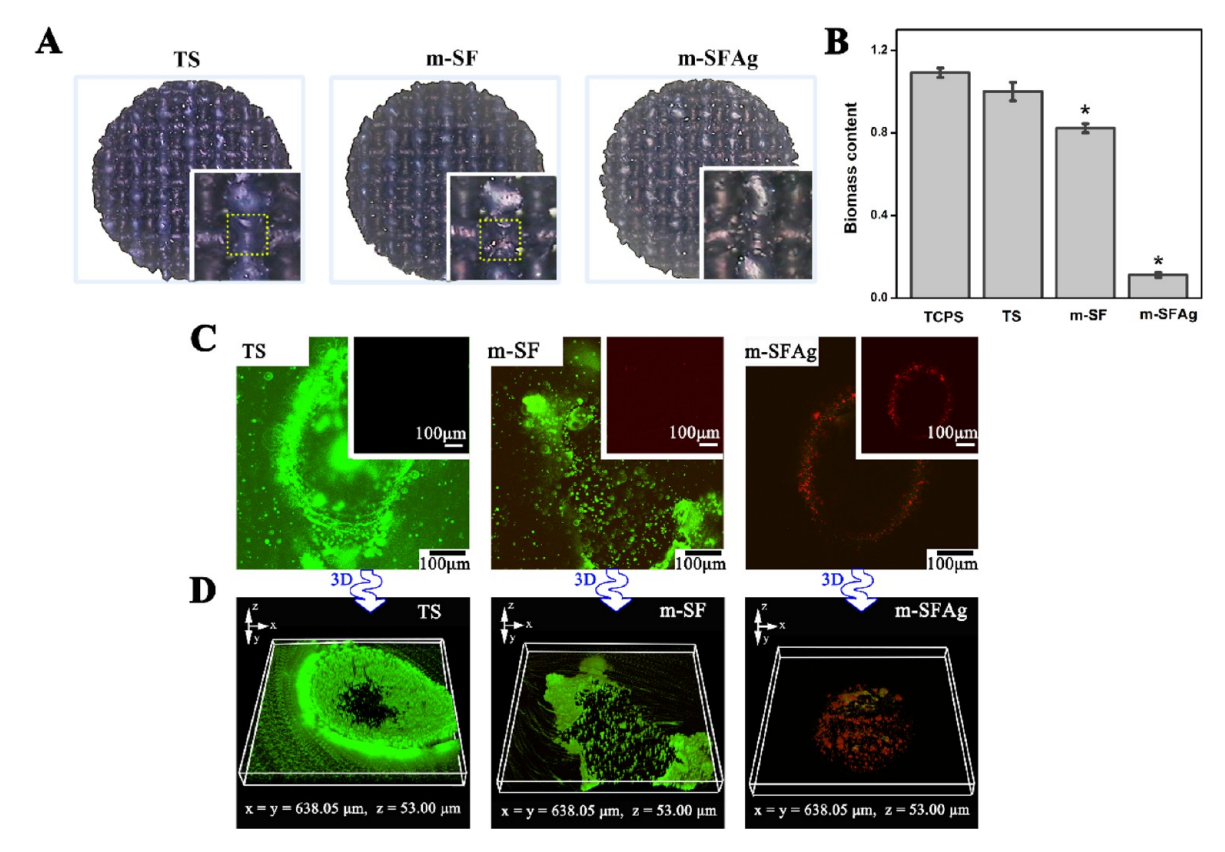


Figure 7. Antibacterial efficacies against *S. aureus* bacteria and plausible mechanisms. (A) Growth curve observation, inset the digital photographs of collected growth media showing turbidity. (B) Inhibition zone assay, inset the digital photographs of representative inhibition zones. (C, D) Antibacterial rates with sustainability against adherent (C) and planktonic (D) bacteria (\*p < 0.05). Hollow and solid bars represent TS and m-SFAg, respectively. (E) In vitro  $Ag^+$  release profiles in PBS ((inset, diagram of release rates). (F) ROS production (\*p < 0.05). (G) Schematic diagram of possible antibacterial factors and their multimode antibacterial actions. There are three major antibacterial factors:  $Ag^+$  ion liberation, ROS overproduction, and surface nanostructure, involving at least one of the following modes of action: (1) membrane damage or rupturing and permeability change, (2) electrostatic interactions, (3) disrupting synthesis of capsular polysaccharides, (4) inhibition of protein synthesis and function, and (5) inhibition of DNA synthesis.

sufficient carboxy groups in SF. They could form strong interaction with  $Ca^{2+}$  ions in SBF, which will further attract  $PO_4^{3-}$  ions around; and due to the supersaturation effects, apatite nucleation and subsequent mineral growth would take place spontaneously. In addition, the underneath titanate layer from hydrothermal pretreatment in alkali might also have contributed to the enhanced apatite nucleation and deposition by means of extensive  $Na^+ - Ca^{2+}$  ionic exchange and through enhancing the overall surface roughness. In these results may

somewhat reflect the in vivo biomineralization trend and osteoconductive activity when implanted into human body, thus helping realizing the potentiality of our scaffolds as bioactive bone-bonding grafts.

Taken together, the as-engineered scaffolds possessed hierarchical biomimetic architecture, super hydrophilicity, and improved bone bioactivity compared to the TS counterparts. Furthermore, our focus was shifted to performance validation experiments including antibacterial and antibiofilm



**Figure 8.** Scaffolds' antibiofilm efficiencies. (A, B) Optical images (A) and biomass quantification (B) of crystal violet stains (\*p < 0.05 vs TS). Yellow rectangles in (A) indicate positively stained biofilm patch areas. (C, D) 2D (C) and 3D (D) CLSM images of bacteria/biofilms by Microbial Live/Dead staining (insets in C, the red fluorescent fields indicating killed bacteria).

studies, and osteocompatibility and osteodifferentiation studies in vitro in vitro, as detailed subsequently.

**3.6.** In Vitro Anti-Infection Functions. 3.6.1. Antibacterial Efficacy and Its Longevity. BAIs are acquired perioperatively, stemming from implant associated biofilms. The key to avoid or mitigate BAIs is to control biofilm before its formation on implant surfaces. It is a well-accepted criterion, in this area, that the latter is realizable through using appropriate chemical and/or physical surface modifications that impair early bacterial attachment in hours perioperatively. 42 Nevertheless, biofunctionalized implant biomaterials with (nearly) absolute killing efficacy and excellent antibacterial sustainability are increasingly demanded in real practice, particularly, concerning the difficulties in healing infective bone defects with chances of endogenic latent infections in the long run.<sup>2,43</sup> Bacterial contamination occurring peri-operatively or hematogenously later remains a significant challenge, which is circumventable neither by antifouling surfaces that will fail upon formation of protein conditioning layers in vivo, nor by continuing prophylactic antibiotic administration given the high risk of developing resistance.44 The scaffold-based prolonged active releasing strategy represents a potent solution.<sup>2</sup> S. aureus bacteria are known as one of the most common causative pathogenic species of BAIs, so they were employed for subsequent antibacterial studies.

As a preliminary assay, the growth curves of *S. aureus* bacterial cultures treated with different scaffolds (TS, m-SF, and m-SFAg) were determined, as shown in Figure 7A. Compared with that of the TS, the growth speed of m-SF treated *S. aureus* cells was not much altered in the initial hours although it was slightly lowered at a later stage. In fact, bacteria

could normally reproduce in both cases, suggesting the TS and m-SFAg scaffolds did not inactivate these pathogens. On the contrary, bacterial growth of microbes treated with m-SFAg was notably inhibited. Just at 2 h, almost all bacterial cells in this group were dead owing to the strong oligodynamic effects of Ag<sup>+</sup> ions. The bacterial growth remained static in the following hours, indicative of durability of these effects.

Alternatively, an inhibition zone test was carried out that intuitively depicts the gross biocidal activity for releasing-active antimicrobial agents. The results are demonstrated in Figure 7B. Clearly, the TS and m-SF did not have any inhibition zone around. This is hardly surprising since these scaffolds themselves endowed little lethality against environmental pathogens, corroborating the growth curve results. In stark contrast, placing the m-SFAg on the top of bacteria-inoculated agar plates led to a distinct inhibition zone with sizes around 19.3 mm wide, indicating that the surrounding bacteria were eradicated. In other words, the silver loaded scaffolds did show appealing antibacterial potencies against clinically important *S. aureus* bacteria.

In addition, the longevity of m-SFAg scaffolds' sterilizing character over time was examined by storage in PBS for up to 6 weeks. Based on spread plate counting, the antibacterial rates against the adhered (i.e.,  $R_{\rm aa}$ ) and planktonic (i.e.,  $R_{\rm ap}$ ) bacteria were determined, with results summarized in Figure 7C, D. Initially, the m-SFAg scaffolds elicited distinctive bactericidal effects with the  $R_{\rm aa}$  value reaching 100%. Factually, almost no adherent or planktonic bacteria survived in this situation. Indeed, antimicrobial capability as such is sufficient to eliminate bacteria as completely as possible and hence avoid the so-called early infections in the first time. More

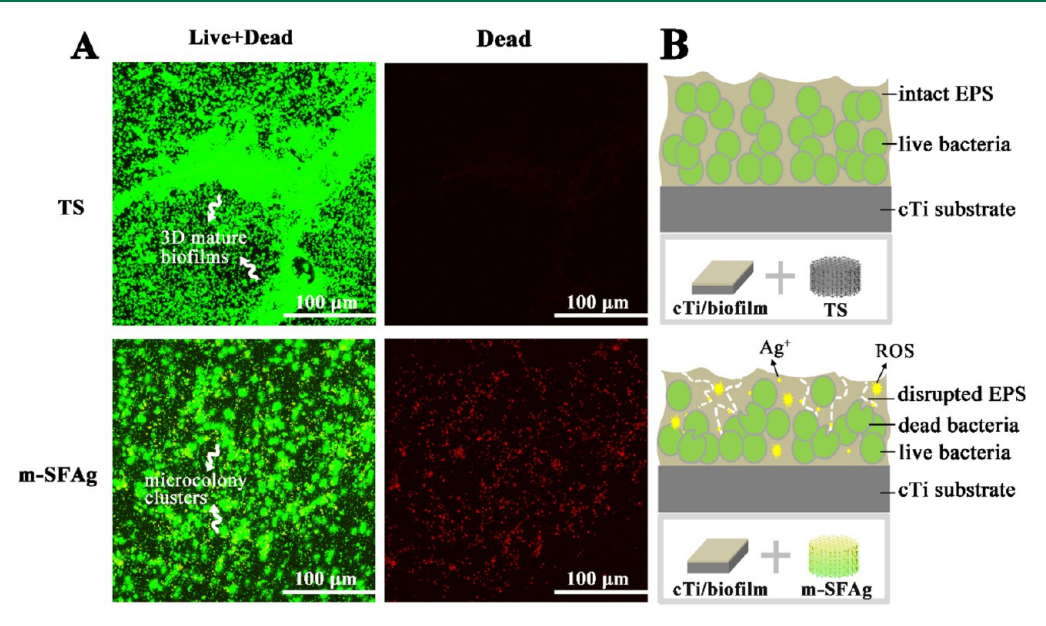


**Figure 9.** Scaffolds' impacts on bacteria within established biofilms during coculture. (A) Typical CLSM fields of the TS/m-SFAg treated biofilms. Note that green overlaps red and yields green yellow. (B) Cartoon schematic of the experimental design and results. Presumably, topical ROS and Ag<sup>+</sup> species arising from m-SFAg scaffolds can diffuse into vicinities of the biofilms and further degrade the biofilm EPS, thus partially exposing the hidden biofilm bacteria and inactivate them.

importantly, that value was maintained for 1 week. The  $R_{aa}$ value decreased marginally from week 2 to week 6, yet ending with over 92%, which is still remarkable for antibacterial materials. For  $R_{\rm ap}$ , its initial value was also ~100%, but it decreased slightly in a week by 7.68%, whereas the following weeks witnessed gradual declines. Nevertheless, the remaining silver was sufficient to elicit a  $R_{\rm ap}$  value of 74.31% by week 6. It is worth noting that the as-tested bacterial concentration (1 × 10<sup>5</sup> CFU mL<sup>-1</sup>) is orders of magnitude higher than real in vivo occasions (1 × 10<sup>2</sup> CFU mL<sup>-1</sup>). Therefore, even higher  $R_{aa}$ and  $R_{\rm ap}$  efficacies are likely to occur under actual conditions. By this justification, we expect our m-SFAg scaffolds to exhibit antiadhesion and bacteria-killing capacities months postoperatively, which would leave plenty of time for potential infection risky factors to be cleared and therefore create a heathy microenvironment favoring bone formation and biointegration.

3.6.2. In Vitro Antibiofilm Property. The major impairment in treating BAIs is identified as the formation of biofilms (adherent dormant bacterial community in self-produced slimy matrix) on implant surface or within bone tissue, which are highly recalcitrant to antibiotic agents and host immune systems. Thereby, it is imperative to equip biomedical devices with both antibacterial and antibiofilm properties.

The antibiofilm property of the scaffolds was determined through exposing them to severe bacteria challenges (1 × 10<sup>8</sup> CFU mL<sup>-1</sup>). After a prolonged harsh cultivation of 2 weeks, specific staining with crystal violet was performed, wherein biofilms were stained bright violet. As disclosed in Figure 8A, uniform violet stains were observed throughout the TS scaffolds, evidencing *S. aureus* biofilm colonization macroscopically on different surfaces. The m-SF samples were also positively stained by random patches of biofilms. In marked contrast, the m-SFAg surfaces remained relatively clear, having few zones of violet color. Meanwhile, the biomass of biofilms was quantified by eluting the stains off the scaffolds (Figure 8B). As compared to the TS, the m-SF slightly retarded biofilm formation by 17.8%. Impressively, through m-SFAg function-

alization, a nearly 90% reduction in biomass was realized. In addition, CLSM-based Live/Dead fluorescent assays were carried out, which can conveniently distinguish microbes with intact and damaged membrane structures as green and red fluorescence, respectively. As shown in Figure 8C, D, large colonies of *S. aureus* bacteria were evidently alive within TS. As to m-SF, sessile biofilms were also prevalent, but with seemingly inhibited growth and appearance of some dead bacteria cells (in red) on the scaffolds. In stark contrast, on m-SFAg there were only tiny spots of scattered, killed *S. aureus* cells.

3.6.3. Ability in Killing Biofilm Bacteria. One of the clinical imperatives in orthopedics stands as the effective regeneration of infective defects such as the extremity open fractures and osteomyelitis-associated defects, wherein free-floating biofilmlike aggregates and/or locally colonized biofilm structures already exist in body fluids, on implant surfaces, or within periimplant tissues.<sup>29,45</sup> The management of these biofilmaccompanied bone defects are challenged, to a large extent, by the fact that microbes sheltered in the slimy and dense biofilm matrix (termed "extracellular polymeric substance, EPS") are orders of magnitude more intractable to be killed using antibiotics in comparison to their individual counterparts. 43 In these cases, the capability of biomaterials to destroy maturely formed biofilms created by virulent bacteria is much more desirable than sole inhibitory effects that deter biofilm formation by individual bacteria.<sup>20</sup>

As such, the capacity of the m-SFAg scaffolds to inactivate or eliminate the biofilm embedded bacteria was evaluated in vitro (Figure 9). A model of *S. aureus* biofilms was constructed first on cTi foils, and then coincubated with TS and m-SFAg to see the effects on biofilm development and microbial viability. CLSM investigation revealed that the living status of bacteria in the TS treated biofilms (control) seemed untouched. To our delight, unlike the TS biofilms, the evolution of the m-SFAg biofilms was retarded and much higher proportion of cell death (stronger red fluorescence) was observed.

3.6.4. Antimicrobial Mechanisms. As is known, nanosilver as a time-honored potent bactericide agent can exert a couple of inherent detrimental toxicity impacts to the survival of bacterial microbes through actively interacting with their membranal structures/components and intracellular substances (enzymes, proteins, RNA/DNA), and involving physical damage, Ag-SH bonds, electrostatic forces, etc. 11,46 These extensive physical or chemical interactions constitute the base of currently available multiple mechanistic pathways of antibacterial AgNPs (Figure 7G), briefly encompassing change of membrane permeability, electrostatic interference, production of free radicals, modulation of phosphotyrosine profiles of proteins, interaction with SH-groups, and suppression of protein/DNA synthesis and functions.46 Succinctly, these antibacterial actions belong to three subjects: nanoparticle itself, ionic silver, and ROS as generated. Admittedly, it still remains elusive touching the accurate toxicity mechanisms of nanosilver toward cells/microorganisms. Nevertheless, for a given silver-based antibacterial surface, the exact mode of action might more likely be clarified, or at least the dominant one can possibly be determined.<sup>2,47</sup>

First, the particle-specific nanotoxicity can virtually be obviated for the following reasoning. In our current study, AgNPs were entirely encapsulated by side chains of silk protein and fully embedded in the SF multilayer, which was then chemically tethered to the scaffold substrate. Thereby, scarcely having particulate surface exposed to bacteria, these Ag particles can hardly elicit contact killing that is known to be mediated by direct physical contacts or Ag–SH bonds. <sup>10</sup> In addition, the Ag particles themselves, with restricted movability, were unlikely to shed off the scaffolds, not to mention traveling through the membrane and thus doing damage to biological contents inside.

On the basis of our antibacterial results, we deduce that Ag+ chemistry was the dominating weapon in our battle against adhesion and growth of S. aureus. On one hand, ionic silver is very prone to bind to the bacterial cell wall/membrane electrostatically and interacts with special groups (e.g., thiol, carboxyl, hydroxyl, amino, phosphate, and imidazole) in proteins and enzymes, thereby disrupting membrane integrity and inducing cell death. 46 On the other, once Ag+ ions cut cross the vulnerable membranal barrier, they would associate with intracellular DNA and biologically essential proteins, and inactivate their activities by suffocation, eventually inhibiting DNA synthesis, respiratory enzymes, and energy transduction.<sup>48</sup> Besides that, Ag<sup>+</sup> can be freed from dead bodies of killed bacteria to attack other survivors by repeating the process above, 49 which is an interesting explanation why silver's killing effect is persistent.

Localized delivery of antibacterial agents at ultrahigh dosage and at the same time, encoding tailored durable release profiles are the key to potentiate strong and sustained bacteria killing efficiency. To interpret the unique capability of  $Ag^+$  ions in bringing strong and sustained antibacterial effects, the silver release profiles were plotted after incubating the scaffolds in PBS (Figure 7E). Delightedly, as high as  $19.87 \pm 1.32~\mu g$  of Ag was immobilized onto each scaffold, as determined by an acid dissolution method. The initial "burst" gave rise to considerably high  $Ag^+$  concentrations (9.9% of total, 1.96  $\mu g^-$  mL<sup>-1</sup>) near the bacteria cell wall and eradicated virtually all the adherent and planktonic bacteria. The releasing continued in following several days and it contributed another 17.5% of the total Ag amount; and afterward a relatively slower but more

steady liberation trend was observed over an extended period up to 42 d. Eventually, there was yet about 40.6% of silver to be released. This explains well the excellent bactericidal persistence in Figure 7C, D. We have reason to believe that the scaffolds' vastly enlarged surface areas macro- and microscopically relative to their solid unmodified counterparts, 1,2,9 served as a unique cargo/reservoir of silver particles/ions, contributing to the locally long-lasting release profiles and thus durable microbe killing performance.

On the other hand, ROS is known an integral part of the nanotoxicity of nanomaterials such as nanosilver. ROS is byproduct of chemical or biochemical processes, which may encompass singlet oxygen, hydroxyl radicals (•OH), peroxides  $(H_2O_2)$ , and superoxide  $(\bullet O_2^-)$ . They are tested as a potent mediator of microbial cell death. ROS exerts overwhelming oxidative stress and targets membranal and cytosolic components and disturbs normal metabolism and replication activities. 46 Excess ROS can be generated in microbes whose electron transport along the mitochondrial respiratory chain is impeded by either particulate Ag or Ag<sup>+</sup> ions. 48,50 The formation of ROS was examined by employing the DCFH-DA fluorescence assay (Figure 7F). Evidently, the m-SFAg group triggered significantly higher ROS levels compared with the others, corroborating the antibacterial role of m-SFAg in mediating oxidative damages. Additionally, ROS is deemed responsible for inactivating biofilm bacteria (Figure 9). It is evidenced that excess ROS is exceptionally able to degrade EPS components such as polysaccharides, proteins, and nucleic acids. 51 Therefore, we speculate that an overwhelming number of free radicals had been generated and liberated in first time and disrupted zones of biofilm EPS, and this allowed Ag+ ions to locally penetrated, counteracting with the vital activities of hidden bacteria and consequently killing them. Such character can be best harnessed if combined with antibiotics to restore infective complicated bone defects, 2,9,48 hence making these scaffolds promising in real clinical adoption, where antibiotics are continuously administrated peri-implantation.

In addition to the known toxic effects of antimicrobials, the micro/nanostructured surface features are assumed to constitute, to a lesser extent, the physical mechanism of antibacterial action through exerting intrinsic impacts on bacteria adhesion and viability. Hitherto, increasing attention has been paid to the intimate relationship between bacteria adherence and biomaterial surface topography. 42,52 Differences in surface landscape/nanotopology often lead to greatly varying bacteria-bacteria and bacteria-biointerface interactions, the rigorous understanding of which has inspired a host of artificial biomaterial surfaces minimizing or resisting fungal attachment or even killing bacteria.<sup>52</sup> In particular, the nanopillar, nanospear and nanowire types of configuration at submicron and microsized length scales possess superior antiadhesion and/or bactericidal activities. 53,555 Here, the m-SF scaffolds retained a relatively smaller number of bacteria relative to the TS, and a few of them lost viability (Figure 8C). Because SF itself does not demonstrate obvious antibacterial property, 20 the underneath nanowire backbone should be responsible. Presumably, the nanowire topography with corresponding sharpness and roughness might have provided unfavorable conditions for bacterial attachment and frustrated a significant portion of them from setting down the scaffold surfaces, thus demonstrating fungal-repealing character. 42 This may in return augment the overall antibacterial effect because free-swimming preys are more vulnerable to Ag+ ions than

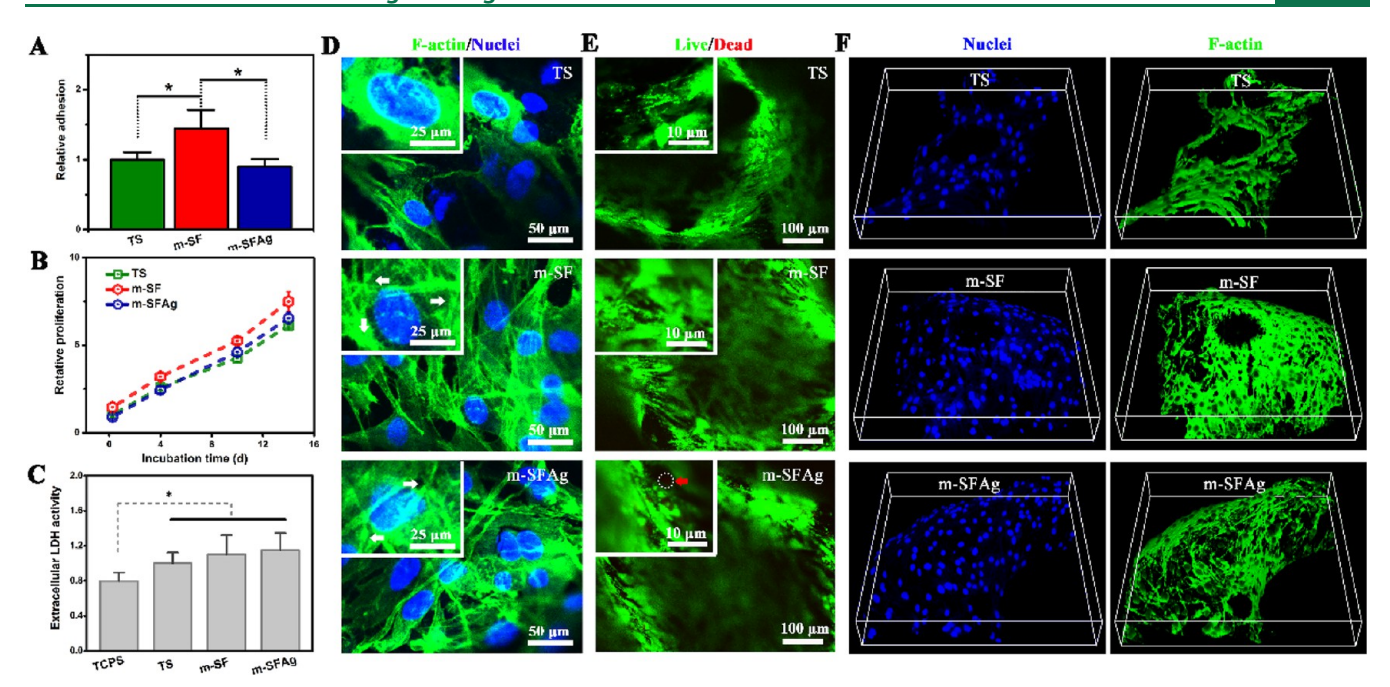


Figure 10. Cytocompatibility of MC3T3-E1 cells toward different scaffolds. (A) Cell adhesion (\*p < 0.05). (B) Cell proliferation profiles. (C) Cytotoxicity measured by extracellular LDH activity (\*p < 0.05). (D) Cytoskeleton development of cells (white arrows point to defined F-actin filaments traveling throughout cell bodies). (E) Cellular Live/Dead staining, inset with enlarged areas of interest (white circle and red arrow indicate PI stained dead cells). (F) Representative 3D reconstructed CLSM images showing the spatial growth and cytoskeletons of osteoblasts within scaffolds.

those firmly cohered to the surface.  $^{56,57}$  It can also explain somehow the antibacterial persistence and why the observed  $R_{\rm aa}$  values stayed more stable over time compared with the  $R_{\rm ap}$ . Moreover, randomly oriented nanowire-type structures can directly deform and puncture microbial membrane, forcing cytoplasm to leak and cells to be lysed.  $^{53-55}$  Nevertheless, these mechanical effects strongly rely on bacteria—surface contacts, hence being unable to kill fungi at a distance by themselves. These effects may also be compromised as bacteria accumulate gradually and biofilms form covering the surface nanostructures.  $^{53}$  Anyway, when such topographical confirmation is combined with AgNPs, the antibiotic arsenal as a whole can be strengthened and the resultant materials would seldom develop drug resistance.

# **3.7.** Osteocompatibility/Osteodifferentiation Studies. *3.7.1.* Osteocompatibility Assessment. For biomaterials incorporated with nanoantimicrobials, apart from the created antibacterial performances, biocompatibility and biosafety issues are equally crucial to and play a key role in clinical adoption of the final biomedical devices. The biocompatibility of the m-SFAg scaffolds were thus assessed in vitro using an osteoblastic culture model of MC3T3-E1, with emphasis on the initial osteoblastic responses to the biomaterials that are the basis of early stage osteogenic functions. In addition, opportunistic bacteria and osteoblastic cells race to adhere, replicate, and colonize on implant surfaces at an early implantation stage, <sup>43</sup> so, favorable initial osteoblastic responses, along with the remarked antibacterial effects, would

best support the host cells to win the competition.

As a first step, the cell adhesion and proliferation of MC3T3-E1 on TS, m-SF, and m-SFAg scaffolds were compared by use of a metabolism-based CCK-8 assay. As demonstrated in Figure 10A, the adherence was increased by 28.2% by the m-SF modification. For m-SFAg, the adherence was significantly

lower than m-SF, however, it was comparable to the TS. As to cell proliferation, a continuous multiplication tendency was noticed for all groups across the investigation period (Figure 10B). In comparison to TS and m-SFAg, at each observation point, the m-SF cells showed the greatest mitochondrial activity, reflecting their superior surface characteristics in supporting faster proliferation. For m-SFAg cells, they did not differ significantly from the TS cells in proliferative activity during the first week. This was probably affected by the initial continuous leakage of inhibitory Ag+ into culture media. Nonetheless, the proliferation for m-SFAg group clearly excelled those for the TS at 14 days, suggesting acceptable biocompatibility at a later stage. Interestingly, unlike the 2D cultures, no plateau stage (indicative of confluence, usually taking 5-7 days for 2D cultures) was reached for all these 3D cultures even at 14 days, embodying the importance of porous scaffold architectures to allow expanding of the cells for desirable bone volume. Additionally, the leakage of intracellular enzyme LDH was examined as an easy indicator of potential cytotoxicity during culture (Figure 10C). Greater amounts of LDH enzyme were found for all material groups compared to negative control. Nonetheless, the LDH leakage for m-SF and m-SFAg groups was just comparable to that of TS, indicative of equivalent levels of cytotoxicity.

In the next step, we examined different scaffolds' abilities in supporting the growth and cytoskeleton development of MC3T3-E1, by means of DAPI and FITC-phalloidin staining coupled with CLSM study (Figure 10D, F). The majority of osteoblasts could normally adhere to, spread, and replicate on all substrate types, but displaying noticeable differences in cell number and morphology. As opposed to TS, greater cell numbers and denser and more organized stress fibers of F-actin were observed on m-SF. More importantly, the cells had developed intertwined stress fibers that spanned across the

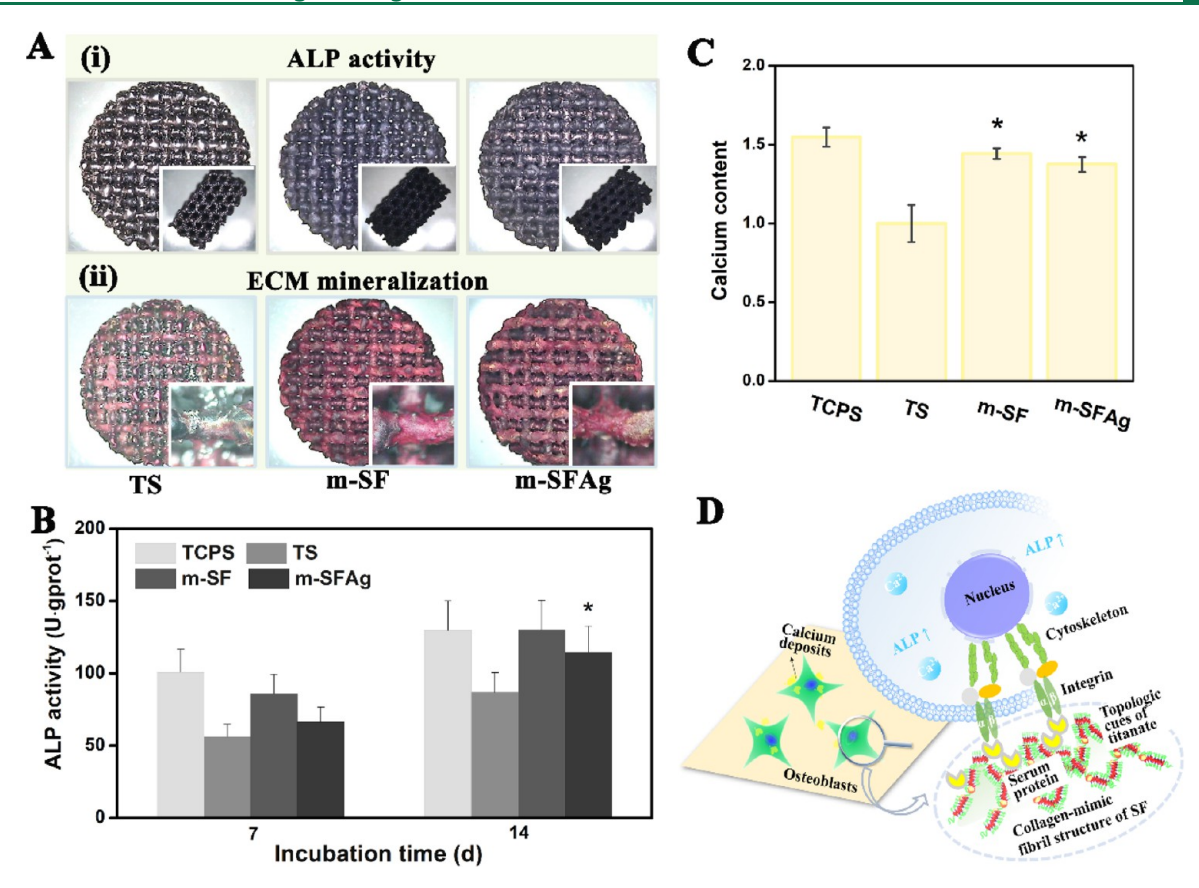


**Figure 11.** In vitro osteodifferentiation activities. (A) BCIP/NBT staining (i) and ARS staining (ii); insets in (i) are side-view pictures illustrating homogeneity of stains throughout scaffold, while insets in (ii) show magnified criss-crossed structs for evidence of calcium nodules. (B) Intracellular ALP activity (\*p < 0.05 vs TS). (C) Quantification of calcium contents (\*p < 0.05 vs TS). (D) Schematic illustration of the biomimetic osteostimulation cues on scaffold surfaces.

scaffold structures in a 3D manner. As for cells cultured on the m-SFAg, no distinguishable difference was found by morphological and cytoskeletal observations, as compared to those on the m-SF. Furthermore, cellular Live/Dead staining was undertaken to visualize the viable status of the cells on various scaffolds (Figure 10E). Live healthy cells appeared green while dead ones were stained red. Generally, compared to the TS, the scaffolds with m-SF and m-SFAg modifications showed better cell status in both quantity and quality with 3D spatial mode of spreading and growth, regardless of the fact that red stained cells were randomly present for m-SFAg cells. These suggest a osteocompatible nature of our materials for long-term implantation utilization.

Note here a special fact of nanosilver, namely, it was embedded within the silk matrix (with eliminated chance of direct exposure) and immobilized onto scaffold surfaces (with restricted movability). Thereby, it is less likely that nanotoxicity induced by cell uptake or direct contact would occur. The initial burst release of Ag<sup>+</sup> ions was to blame first for retarded adhesion and death of m-SFAg cells in early cultivation. Nevertheless, the cell metabolism improved gradually with time, presumably as a consequence of several factors. First, the release kinetics in Figure 7E comprised gradual decreasing rates of silver leakage and thus limited silver was there at later stages. Second, ligands of Ag<sup>+</sup> in the medium (serum proteins, anions like Cl<sup>-</sup>, and degraded silk molecules, if any) can provide a number of binding sites to free Ag<sup>+</sup> ions, hence greatly reducing the bioavailability of unfavorable Ag<sup>+</sup>. Third, excess harmful Ag species were scavenged

along with old medium by refreshment, so the toxicity was relieved accordingly.<sup>2</sup> Another thing deserving attention is that our AgNPs were in a unique "Ag core/SF corona" form (Figure 4A) rather than simply naked, as is common in prior studies.<sup>1,8,44</sup> We were delighted to find that for surface immobilized AgNPs, their cytocompatibility clearly improved when they were gradually covered with an ECM corona layer (majorly collagen proteins) formed during culture.<sup>10</sup> Xu et al. also confirmed that a capping layer of chitosan lowered the negative effects of AgNPs.<sup>39</sup> In essence, silk is a biopolymer similar to the collagen and chitosan, so expectedly, a corona layer of it on nanosilver should exert a positive impact on the overall biocompatibility. Given any other unfavorable aspects of silver, they can be compensated by several cell-assisting surface characteristics, as will be discussed below.

3.7.2. Osteogenic Differentiation Functions. The differentiating of osteoblastic cells such as MC3T3-E1 is correlated with the deposition of bone matrix, which is of utmost significance in maintaining normal skeletal architectures and establishing tight osseointegration during regeneration. To this end, MC3T3-E1 cells were seeded onto our scaffolds and cultivated for up to 28 days, and ALP activity and ECM mineralization were evaluated in vitro as hallmarkers of early and late stage osteodifferentiation, respectively.

ALP is a key enzyme fostering early bone formation through providing an alkaline microenvironment and high concentrations of phosphate around the mineral deposition sites. All the scaffold species supported MC3T3-E1 differentiation, with evident intracellular ALP enzyme expression (Figure 11B).

Particularly, the m-SF showed the highest ALP activities during the entire culture among all material groups. There was, however, no significant difference (p > 0.05) in ALP between the TS and m-SFAg cells until 14 d. The ALP directed early osteodifferentiation was further evidenced by BCIP/NBT staining (Figure 11A-i), which is capable of visualizing the overall intracellular ALP contents. Noticeably, the ALP stains on m-SF and m-SFAg scaffolds, especially the m-SF, were darker than that on TS, agreeing with the ALP tests above.

The degree of ECM mineralization is identified as a latestage osteogenic differentiation marker, and mineralized ECM serves as a basic block for building hierarchically organized bone structures. We examined the ECM mineralization through ARS-Ca<sup>2+</sup> staining. First, judging from the optical images in Figure 11A-ii, all scaffolds were stained positive (red), but the m-SF and m-SFAg stains were darker and more uniform throughout the scaffolds relative to the TS, suggesting the occurrence of much stronger and more homogeneous mineralization. Quantitative analysis of the eluted stains revealed an akin trend as the ALP assays (Figure 11C), i.e., the m-SF surface induced the highest degree of matrix mineralization, followed by m-SFAg. In other words, the titanate nanowire/silk-based biomimetic functionalization, regardless of silver immobilization, markedly enhanced the osteogenicity of as-manufactured scaffolds.

The clinical success of artificial scaffolds to correct or reconstruct defected bone is governed by the scaffolds' macroscopic architecture and surface properties at micro/ nanoscale. Macroscopically speaking, the grafts ought to present fully open porous structures that allow easy ingrowth of bone tissues and blood vessels and facilitate mass transport and nutrient supply.<sup>1,5</sup> From an osteogenic point of view, micro/nanoscaled biomimicry and compositional similarity to the ECM of native bone should ideally be encompassed or created for a biomaterial to direct cellular attachment, proliferation, and migration, and elicit suitable osteostimulative biophysical/chemical signals. 10,14 In the present study, 3D porous implant microarchitecture exhibiting considerably high porosity (~73%) and excellent interconnectivity were endangered via 3D printing to meet the first criterion. In considering the ECM-mimicking osteogenic features, titanate nanowire/silk protein based composite coatings were subsequently engineered post fabrication. As schematically illustrated in Figure 11D, silk polymer is very able to facilitate osteogenesis by resembling the elaborate structural and chemical contents of ECM collagen protein. 16,17 Meanwhile, the micro/nanostructure conferred by the nanowire scaffold is assumed to provide an "immense" 3D microenvironment for osteoblast adhesion, proliferation, and differentiation.<sup>27</sup> Physical stimulation from the surface roughness and nanowire landscape as well should have great influence on the cellmaterial interactions and intercommunication among the cells, which may dominate the fate of bone-forming cells for osteodifferentiation and maturation.<sup>38,58</sup> Grossly increased bioactivity improves bone/implant integration.3 Pleasingly, greater bioactivity capacity was verified on the functionalized scaffolds by our in vitro apatite formation test in SBF (Figure 6C). This may correspond to accelerated bone matrix deposition and tissue fixation in vivo. Importantly, the above osteogenic aspects were maintained or did not deteriorate much when silver was immobilized. All these data, coupled with the antibacterial and anti-infection functionalities, would support our m-SFAg scaffolds in repairing bone defects

challenged by bacterial contaminations, through scavenging the pathogens and orchestrating the healing process.

#### 4. CONCLUSIONS

In this research, hierarchically biomimetic 3D porous titanium scaffolds with osteogenic and anti-infection bifunctionalities were produced through ingeniously syncretizing the emerging 3D printing principle with a titanate/silk protein/Ag biofunctionalization strategy. Briefly, macroporous titanium was first tailor-made by metallic powder 3D printing and subjected to in situ hydrothermal growth of a micro/nanostructured titanate layer, to which nanosilver encapsulated, physically cross-linked SF multilayers were anchored through PDA-assisted, silk-on-silk self-assembly. By this means, we easily altered the hydrophilicity, protein affinity, and bioactivity of the primary bare bioinert metal substrate and imparted micro/nanotopographical and biochemical cues to the constructs simultaneously.

Using the resultant scaffolds, strong yet sustained sterilizing effects were achieved against either planktonic or adherent S. aureus bacteria in a 6 weeks' durability challenge. Additionally, these scaffolds not merely defended themselves efficaciously from biofilm colonization, but also killed a notable number of dormant bacteria entombed in already established biofilms. Active Ag+ release and overwhelming oxidative stress were evidenced as principal antibacterial mechanisms. Further, the biocompatibility of these scaffolds was revealed generally acceptable in MC3TE3-E1 osteoblast cultures and impressive osteogenic functionality was elicited in the long run. These aspects, together with the huge advantages of freedom in design, easiness of fabrication, appreciable mechanical compatibility with bone, and inexpensive production, bode well for long-term osteo-implantation application that targets at healing shape-complicated and bacteria-associated defects. Nevertheless, optimization of material fabrication is demanded, as well as further animal studies to test in vivo performances and relieve biosafety concerns.

#### ASSOCIATED CONTENT

# Supporting Information

The Supporting Information is available free of charge on the ACS Publications Web site at The Supporting Information is available free of charge on the ACS Publications website at DOI: 10.1021/acsbiomaterials.8b00857.

Appearances of SFAg composites at varying Ag contents, schematic of the EBM system, gross observations of TS samples, morphological evolution of nanotitanate over time, and samples constructed at alternative SF concentrations and assembly cycles (PDF)

#### AUTHOR INFORMATION

# **Corresponding Authors**

\*Y. Z. Tel & Fax: +86-10-6276 7411. E-mail: yfzheng@pku. edu.cn.

\*Y. C. Tel & Fax: +86-10-62753404. E-mail: chengyan@pku. edu.cn.

## ORCID ®

Yan Cheng: 0000-0001-7956-9395 Yufeng Zheng: 0000-0002-7402-9979

#### Notes

The authors declare no competing financial interest.

#### ACKNOWLEDGMENTS

This work was supported by the National Natural Science Foundation of China (Grant 51431002 and 51871004), NSFC/RGC Joint Research Scheme (Grant 5161101031) and National Key Research and Development Program of China (Grant 2016YFC1102402).

### REFERENCES

- (1) Amin Yavari, S.; Loozen, L.; Paganelli, F. L.; Bakhshandeh, S.; Lietaert, K.; Groot, J. A.; Fluit, A. C.; Boel, C. H.; Alblas, J.; Vogely, H. C.; Weinans, H.; Zadpoor, A. A. Antibacterial Behavior of Additively Manufactured Porous Titanium with Nanotubular Surfaces Releasing Silver Ions. ACS Appl. Mater. Interfaces 2016, 8, 17080–17089.
- (2) Jia, Z. J.; Xiu, P.; Xiong, P.; Zhou, W. H.; Cheng, Y.; Wei, S. C.; Zheng, Y. F.; Xi, T. F.; Cai, H.; Liu, Z. J.; Wang, C. M.; Zhang, W. P.; Li, Z. J. Additively Manufactured Macroporous Titanium with Silver-Releasing Micro-/Nanoporous Surface for Multipurpose Infection Control and Bone Repair A Proof of Concept. ACS Appl. Mater. Interfaces 2016, 8 (42), 28495–28510.
- (3) Amin Yavari, S.; van der Stok, J.; Chai, Y. C.; Wauthle, R.; Tahmasebi Birgani, Z.; Habibovic, P.; Mulier, M.; Schrooten, J.; Weinans, H.; Zadpoor, A. A. Bone Regeneration Performance of Surface-Treated Porous Titanium. *Biomaterials* **2014**, 35, 6172–6181.
- (4) Arabnejad, S.; Johnston, B.; Tanzer, M.; Pasini, D. Fully Porous 3D Printed Titanium Femoral Stem to Reduce Stress-Shielding Following Total Hip Arthroplasty. *J. Orthop. Res.* **2017**, *35*, 1774–1783.
- (5) Shah, F. A.; Snis, A.; Matic, A.; Thomsen, P.; Palmquist, A. 3D printed Ti6Al4V Implant Surface Promotes Bone Maturation and Retains a Higher Density of Less Aged Osteocytes at The Bone-Implant Interface. *Acta Biomater.* **2016**, *30*, 357–367.
- (6) Raphel, J.; Holodniy, M.; Goodman, S. B.; Heilshorn, S. C. Multifunctional Coatings to Simultaneously Promote Osseointegration and Prevent Infection of Orthopaedic Implants. *Biomaterials* **2016**, *84*, 301–314.
- (7) Inzana, J. A.; Schwarz, E. M.; Kates, S. L.; Awad, H. A. Biomaterials Approaches to Treating Implant-Associated Osteomyelitis. *Biomaterials* **2016**, *81*, 58–71.
- (8) van Hengel, I. A. J.; Riool, M.; Fratila-Apachitei, L. E.; Witte-Bouma, J.; Farrell, E.; Zadpoor, A. A.; Zaat, S. A. J.; Apachitei, I. Selective Laser Melting Porous Metallic Implants with Immobilized Silver Nanoparticles Kill and Prevent Biofilm Formation by Methicillin-Resistant Staphylococcus Aureus. *Biomaterials* 2017, 140, 1–15
- (9) Bakhshandeh, S.; Gorgin Karaji, Z.; Lietaert, K.; Fluit, A. C.; Boel, C. H. E.; Vogely, H. C.; Vermonden, T.; Hennink, W. E.; Weinans, H.; Zadpoor, A. A.; Amin Yavari, S. Simultaneous Delivery of Multiple Antibacterial Agents from Additively Manufactured Porous Biomaterials to Fully Eradicate Planktonic and Adherent Staphylococcus Aureus. ACS Appl. Mater. Interfaces 2017, 9, 25691–25699.
- (10) Jia, Z. J.; Xiu, P.; Li, M.; Xu, X. C.; Shi, Y. Y.; Cheng, Y.; Wei, S. C.; Zheng, Y. F.; Xi, T. F.; Cai, H.; Liu, Z. J. Bioinspired Anchoring AgNPs onto Micro-Nanoporous TiO2 Orthopedic Coatings: Trapkilling of Bacteria, Surface-Regulated Osteoblast Functions and Host Responses. *Biomaterials* **2016**, *75*, 203–222.
- (11) Eckhardt, S.; Brunetto, P. S.; Gagnon, J.; Priebe, M.; Giese, B.; Fromm, K. M. Nanobio Silver: Its Interactions with Peptides and Bacteria, and its Uses in Medicine. *Chem. Rev.* **2013**, *113*, 4708–4754.
- (12) Bai, S.; Liu, S.; Zhang, C.; Xu, W.; Lu, Q.; Han, H.; Kaplan, D. L.; Zhu, H. Controllable Transition of Silk Fibroin Nanostructures: An Insight into in Vitro Silk Self-Assembly Process. *Acta Biomater.* **2013**, *9*, 7806–7813.
- (13) Rockwood, D. N.; Preda, R. C.; Yucel, T.; Wang, X. Q.; Lovett, M. L.; Kaplan, D. L. Materials Fabrication from Bombyx Mori Silk Fibroin. *Nat. Protoc.* **2011**, *6*, 1612–1631.

- (14) Mottaghitalab, F.; Hosseinkhani, H.; Shokrgozar, M. A.; Mao, C. B.; Yang, M. Y.; Farokhi, M. Silk as a Potential Candidate for Bone Tissue Engineering. *J. Controlled Release* **2015**, 215, 112–128.
- (15) Lin, F.; Li, Y.; Jin, J.; Cai, Y.; Wei, K.; Yao, J. Deposition Behavior and Properties of Silk Fibroin Scaffolds Soaked in Simulated Body Fluid. *Mater. Chem. Phys.* **2008**, *111*, 92–97.
- (16) Marelli, B.; Ghezzi, C. E.; Alessandrino, A.; Barralet, J. E.; Freddi, G.; Nazhat, S. N. Silk Fibroin Derived Polypeptide-Induced Biomineralization of Collagen. *Biomaterials* **2012**, *33*, 102–108.
- (17) Midha, S.; Murab, S.; Ghosh, S. Osteogenic Signaling on Silk-Based Matrices. *Biomaterials* **2016**, *97*, 133–153.
- (18) Han, C. J.; Yao, Y.; Cheng, X.; Luo, J. X.; Luo, P.; Wang, Q.; Yang, F.; Wei, Q. S.; Zhang, Z. Electrophoretic Deposition of Gentamicin-Loaded Silk Fibroin Coatings on 3D-Printed Porous Cobalt-Chromium-Molybdenum Bone Substitutes to Prevent Orthopedic Implant Infections. *Biomacromolecules* **2017**, *18*, 3776–3787.
- (19) Sun, J. C.; Zhang, Y. X.; Li, B.; Gu, Y.; Chen, L. Controlled Release of BMP-2 from a Collagen-Mimetic Peptide-Modified Silk Fibroin-Nanohydroxyapatite Scaffold for Bone Regeneration. *J. Mater. Chem. B* **2017**, *5*, 8770–8779.
- (20) Fei, X.; Jia, M.; Du, X.; Yang, Y.; Zhang, R.; Shao, Z.; Zhao, X.; Chen, X. Green Synthesis of Silk Fibroin-Silver Nanoparticle Composites with Effective Antibacterial and Biofilm-Disrupting Properties. *Biomacromolecules* **2013**, *14*, 4483–4488.
- (21) Kharlampieva, E.; Zimnitsky, D.; Gupta, M.; Bergman, K. N.; Kaplan, D. L.; Naik, R. R.; Tsukruk, V. V. Redox-Active Ultrathin Template of Silk Fibroin: Effect of Secondary Structure on Gold Nanoparticle Reduction. *Chem. Mater.* **2009**, *21*, 2696–2704.
- (22) Shchepelina, O.; Drachuk, I.; Gupta, M. K.; Lin, J.; Tsukruk, V. V. Silk-on-Silk Layer-by-Layer Microcapsules. *Adv. Mater.* **2011**, 23, 4655–4660.
- (23) Lee, H.; Dellatore, S. M.; Miller, W. M.; Messersmith, P. B. Mussel-Inspired Surface Chemistry for Multifunctional Coatings. *Science* **2007**, *318* (5849), 426–430.
- (24) Liu, Y. L.; Ai, K. L.; Lu, L. H. Polydopamine and Its Derivative Materials: Synthesis and Promising Applications in Energy, Environmental, and Biomedical Fields. *Chem. Rev.* **2014**, *114*, 5057–5115.
- (25) Zhou, W.; Jia, Z.; Xiong, P.; Yan, J.; Li, Y.; Li, M.; Cheng, Y.; Zheng, Y. Bioinspired and Biomimetic AgNPs/Gentamicin-Embedded Silk Fibroin Coatings for Robust Antibacterial and Osteogenetic Applications. ACS Appl. Mater. Interfaces 2017, 9, 25830–25846.
- (26) Wang, X.; Gu, Z. P.; Jiang, B.; Li, L.; Yu, X. X. Surface Modification of Strontium-Doped Porous Bioactive Ceramic Scaffolds via Poly(DOPA) Coating and Immobilizing Silk Fibroin for Excellent Angiogenic and Osteogenic Properties. *Biomater. Sci.* **2016**, *4*, 678–688.
- (27) Dong, W.; Zhang, T.; Epstein, J.; Cooney, L.; Wang, H.; Li, Y.; Jiang, Y. B.; Cogbill, A.; Varadan, V.; Tian, Z. R. Multifunctional Nanowire Bioscaffolds on Titanium. *Chem. Mater.* **2007**, *19*, 4454–4459
- (28) Kokubo, T.; Takadama, H. How Useful is SBF in Predicting in Vivo Bone Bioactivity? *Biomaterials* **2006**, 27, 2907–2915.
- (29) Wang, J.; Li, J.; Qian, S.; Guo, G.; Wang, Q.; Tang, J.; Shen, H.; Liu, X.; Zhang, X.; Chu, P. K. Antibacterial Surface Design of Titanium-Based Biomaterials for Enhanced Bacteria-Killing and Cell-Assisting Functions Against Periprosthetic Joint Infection. ACS Appl. Mater. Interfaces 2016, 8, 11162–1178.
- (30) Jia, Ž.; Shi, Y.; Xiong, P.; Zhou, W.; Cheng, Y.; Zheng, Y.; Xi, T.; Wei, S. From Solution to Biointerface: Graphene Self-Assemblies of Varying Lateral Sizes and Surface Properties for Biofilm Control and Osteodifferentiation. ACS Appl. Mater. Interfaces 2016, 8, 17151–17165.
- (31) Yu, K.; Lu, F.; Li, Q.; Chen, H.; Lu, B.; Liu, J.; Li, Z.; Dai, F.; Wu, D.; Lan, G. In Situ Assembly of Ag Nanoparticles (AgNPs) on Porous Silkworm Cocoon-Based Would Film: Enhanced Antimicrobial and Wound Healing Activity. *Sci. Rep.* **2017**, *7*, 2107.
- (32) Jiang, C. Y.; Wang, X. Y.; Gunawidjaja, R.; Lin, Y. H.; Gupta, M. K.; Kaplan, D. L.; Naik, R. R.; Tsukruk, V. V. Mechanical

- Properties of Robust Ultrathin Silk Fibroin Films. Adv. Funct. Mater. 2007, 17, 2229–2237.
- (33) Yin, Y.; Hu, K.; Grant, A. M.; Zhang, Y.; Tsukruk, V. V. Biopolymeric Nanocomposites with Enhanced Interphases. *Langmuir* **2015**, *31* (39), 10859–10870.
- (34) Nam, J.; Park, Y. H. Morphology of Regenerated Silk Fibroin: Effects of Freezing Temperature, Alcohol Addition, and Molecular Weight. *J. Appl. Polym. Sci.* **2001**, *81*, 3008–3021.
- (35) Zhang, K.; Feng, Q.; Xu, J.; Xu, X.; Tian, F.; Yeung, K. W. K.; Bian, L. Self-Assembled Injectable Nanocomposite Hydrogels Stabilized by Bisphosphonate-Magnesium (Mg<sup>2+</sup>) Coordination Regulates the Differentiation of Encapsulated Stem Cells via Dual Crosslinking. *Adv. Funct. Mater.* **2017**, *27*, 1701642.
- (36) Ramani, R.; Hanski, S.; Laiho, A.; Tuma, R.; Kilpelainen, S.; Tuomisto, F.; Ruokolainen, J.; Ikkala, O. Evidence of PPII-Like Helical Conformation and Glass Transition in a Self-Assembled Solid-State Polypeptide-Surfactant Complex: Poly(L-Histidine)/Docylbenzenesulfonic Acid. *Biomacromolecules* **2008**, *9*, 1390–1397.
- (37) Marelli, B.; Patel, N.; Duggan, T.; Perotto, G.; Shirman, E.; Li, C. M.; Kaplan, D. L.; Omenetto, F. G. Programming Function into Mechanical Forms by Directed Assembly of Silk Bulk Materials. *Proc. Natl. Acad. Sci. U. S. A.* **2017**, *114*, 451–456.
- (38) Rosales-Leal, J. I.; Rodriguez-Valverde, M. A.; Mazzaglia, G.; Ramon-Torregrosa, P. J.; Diaz-Rodriguez, L.; Garcia-Martinez, O.; Vallecillo-Capilla, M.; Ruiz, C.; Cabrerizo-Vilchez, M. A. Effect of Roughness, Wettability and Morphology of Engineered Titanium Surfaces on Osteoblast-Like Cell Adhesion. *Colloids Surf., A* **2010**, 365, 222–229.
- (39) Xu, Z.; Li, M.; Li, X.; Liu, X.; Ma, F.; Wu, S.; Yeung, K. W.; Han, Y.; Chu, P. K. Antibacterial Activity of Silver Doped Titanate Nanowires on Ti Implants. ACS Appl. Mater. Interfaces 2016, 8, 16584–16594.
- (40) Li, J. H.; Zhang, W. J.; Qiao, Y. Q.; Zhu, H. Q.; Jiang, X. Q.; Liu, X. Y.; Ding, C. X. Chemically Regulated Bioactive Ion Delivery Platform on a Titanium Surface for Sustained Controlled Release. *J. Mater. Chem. B* **2014**, *2*, 283–294.
- (41) Zavgorodniy, A. V.; Borrero-Lopez, O.; Hoffman, M.; LeGeros, R. Z.; Rohanizadeh, R. Mechanical Stability of Two-Step Chemically Deposited Hydroxyapatite Coating on Ti Substrate: Effects of Various Surface Pretreatments. J. Biomed. Mater. Res., Part B 2011, 99b, 58–69
- (42) Meng, J. X.; Zhang, P. C.; Wang, S. T. Recent Progress in Biointerfaces with Controlled Bacterial Adhesion by Using Chemical and Physical Methods. *Chem. Asian J.* **2014**, *9*, 2004–2016.
- (43) Busscher, H. J.; van der Mei, H. C.; Subbiahdoss, G.; Jutte, P. C.; van den Dungen, J. J.; Zaat, S. A.; Schultz, M. J.; Grainger, D. W. Biomaterial-Associated Infection: Locating the Finish Line in the Race for the Surface. *Sci. Transl. Med.* **2012**, *4*, 153rv10.
- (44) Qin, H.; Cao, H. L.; Zhao, Y. C.; Zhu, C.; Cheng, T.; Wang, Q. J.; Peng, X. C.; Cheng, M. Q.; Wang, J. X.; Jin, G. D.; Jiang, Y.; Zhang, X. L.; Liu, X. Y.; Chu, P. K. In Vitro and in Vivo Anti-Biofilm Effects of Silver Nanoparticles Immobilized on Titanium. *Biomaterials* **2014**, 35, 9114–9125.
- (45) Dastgheyb, S.; Parvizi, J.; Shapiro, I. M.; Hickok, N. J.; Otto, M. Effect of Biofilms on Recalcitrance of Staphylococcal Joint Infection to Antibiotic Treatment. *J. Infect. Dis.* **2015**, *211*, 641–650.
- (46) Duran, N.; Duran, M.; de Jesus, M. B.; Seabra, A. B.; Favaro, W. J.; Nakazato, G. Silver Nanoparticles: A New View on Mechanistic Aspects on Antimicrobial Activity. *Nanomedicine* **2016**, *12*, 789–799.
- (47) Song, Y. Y.; Jiang, H. J.; Wang, B. B.; Kong, Y.; Chen, J. Silver-Incorporated Mussel-Inspired Polydopamine Coatings on Mesoporous Silica as an Efficient Nanocatalyst and Antimicrobial Agent. ACS Appl. Mater. Interfaces 2018, 10, 1792–1801.
- (48) Morones-Ramirez, J. R.; Winkler, J. A.; Spina, C. S.; Collins, J. J. Silver Enhances Antibiotic Activity Against Gram-Negative Bacteria. Sci. Transl. Med. 2013, 5, 190ra81.
- (49) Wakshlak, R. B.; Pedahzur, R.; Avnir, D. Antibacterial Activity of Silver-Killed Bacteria: The "Zombies" Effect. *Sci. Rep.* **2015**, *5*, 9555.

- (50) Su, H. L.; Chou, C. C.; Hung, D. J.; Lin, S. H.; Pao, I. C.; Lin, J. H.; Huang, F. L.; Dong, R. X.; Lin, J. J. The Disruption of Bacterial Membrane Integrity through ROS Generation Induced by Nanohybrids of Silver and Clay. *Biomaterials* **2009**, *30*, 5979–5987.
- (51) Bing, W.; Chen, Z. W.; Sun, H. J.; Shi, P.; Gao, N.; Ren, J. S.; Qu, X. G. Visible-Light-Driven Enhanced Antibacterial and Biofilm Elimination Activity of Graphitic Carbon Nitride by Embedded Ag Nanoparticles. *Nano Res.* **2015**, *8*, 1648–1658.
- (52) Hasan, J.; Chatterjee, K. Recent Advances in Engineering Topography Mediated Antibacterial Surfaces. *Nanoscale* **2015**, *7*, 15568–15575.
- (53) Cao, Y.; Su, B.; Chinnaraj, S.; Jana, S.; Bowen, L.; Charlton, S.; Duan, P.; Jakubovics, N. S.; Chen, J. Nanostructured Titanium Surfaces Exhibit Recalcitrance towards Staphylococcus Epidermidis Biofilm Formation. *Sci. Rep.* **2018**, *8*, 1071.
- (54) Ivanova, E. P.; Hasan, J.; Webb, H. K.; Gervinskas, G.; Juodkazis, S.; Truong, V. K.; Wu, A. H. F.; Lamb, R. N.; Baulin, V. A.; Watson, G. S.; Watson, J. A.; Mainwaring, D. E.; Crawford, R. J. Bactericidal Activity of Black Silicon. *Nat. Commun.* **2013**, *4*, 2838.
- (55) Hasan, J.; Jain, S.; Chatterjee, K. Nanoscale Topography on Black Titanium Imparts Multi-Biofunctional Properties for Orthopedic Applications. *Sci. Rep.* **2017**, *7*, 41118.
- (56) Gbejuade, H. O.; Lovering, A. M.; Webb, J. C. The Role of Microbial Biofilms in Prosthetic Joint Infections. *Acta Orthop.* **2015**, *86*, 147–158.
- (57) Olsen, I. Biofilm-Specific Antibiotic Tolerance and Resistance. *Eur. J. Clin. Microbiol. Infect. Dis.* **2015**, 34, 877–886.
- (58) Wu, G.; Li, P.; Feng, H.; Zhang, X.; Chu, P. K. Engineering and Functionalization of Biomaterials via Surface Modification. *J. Mater. Chem. B* **2015**, *3*, 2024–2042.